Journal of *Marine Science and Engineering*

MDPI

Article

Hydrodynamic Loads on a Group of Six Structures of Different Cross-Sections in Uniform and Sheared Flow

Henry Francis Annapeh [1] and Victoria Kurushina [1,2,*]

[1] Laboratory of Vibration and Hydrodynamic Modelling, Industrial University of Tyumen, 38 Volodarskogo Street, 625000 Tyumen, Russia
[2] School of Engineering, Newcastle University, Newcastle upon Tyne NE1 7RU, UK
* Correspondence: v.kurushina@outlook.com

Abstract: The estimates of hydrodynamic forces for a group of structures represent a challenge for the design of offshore systems, as they are subject to changes with a variation in flow profiles. The fluctuating effects may be more pronounced or, on the contrary, suppressed if the cross-sectional shape of structures in an array is altered. The present work performs a series of 2D numerical simulations for the flow past six identical stationary cylinders of three distinct geometrical shapes arranged in a 2 × 3 matrix configuration. The flow profiles considered have an averaged velocity corresponding to the critical flow regime of a Reynolds number of 2.5×10^5. The detached eddy simulation k–ω SST turbulence model is employed to perform a comprehensive investigation of the fluid force coefficients, their frequencies and vortex formation patterns. The effect of the spacing ratio varied simultaneously among the structures from 2 to 7 is considered in conjunction with the change in the flow profile and the cylinders' cross-section. The results of simulations show a higher mean drag on the upstream cylinders, reduced mean drag on the mid- and downstream cylinders with the second cross-sectional shape, and a higher mean drag on the cylinders with the third cross-sectional shape, compared to the original circular cylinders.

Keywords: hydrodynamic forces; vortex-induced loads; uniform flow; planar sheared flow; drag coefficient; lift coefficient

Citation: Annapeh, H.F.; Kurushina, V. Hydrodynamic Loads on a Group of Six Structures of Different Cross-Sections in Uniform and Sheared Flow. *J. Mar. Sci. Eng.* **2023**, *11*, 383. https://doi.org/10.3390/jmse11020383

Academic Editor: Abdellatif Ouahsine

Received: 25 December 2022
Revised: 23 January 2023
Accepted: 3 February 2023
Published: 9 February 2023

1. Introduction

The layout of offshore systems for renewable energy harvesting, carbon storage, and production of fossil fuels often involves a complex combination of stationary and moving, rigid and flexible structures placed in proximity to each other. Slender structures represent a specific case of vulnerability to the effects of the vortex formation along the free spans, while these elements may be intended to reach deepwaters and, hence, require extended lengths. Design challenges arise from the number of structures, distances among them, variations in cross-sectional shapes, sizes, and velocity of the flow, which naturally exhibits a 3D complexity.

Several structures arranged in a group are first considered in experimental and modelling research as a couple of identical cylinders in side-by-side, tandem and staggered configurations. The fundamental work [1] investigates the flow around two circular stationary cylinders in tandem and identifies three flow regimes based on the centre-to-centre spacing ratio L/D (where L is the distance between the centres of cylinders and D is the cylinder diameter). The extended-body regime is identified at $1.0 < L/D < 1.8$ and stands for the merging of wakes behind two structures, with a single vortex street forming behind the downstream object. The reattachment regime at $1.8 \leq L/D \leq 3.8$ is distinguished based on the observation of shear layers shedding from the upstream cylinder and reattaching to the face of the downstream cylinder, and the vortex shedding is observed only in the wake of the downstream cylinder. Finally, the co-shedding regime is found at $L/D > 3.8$, where two separate vortex streets are clearly formed, with a partial wake interference

around the downstream structure. These basic flow regimes underly the processes of vortex formation in the cases of more complex geometrical arrangements of stationary and moving structures.

A detailed study on the vortex interaction for cylinders in tandem is performed in [2,3]. The effect of the spacing on flow-induced vibrations (FIV) of two tandem circular cylinders at subcritical Reynolds numbers is studied numerically in [4]. The concept of wake stiffness, affecting hydrodynamic loads and resulting vibration of the downstream structure in tandem, is discussed in [5]. In [6], experiments with two staggered circular cylinders of equal diameter are performed in order to measure the vortex shedding frequencies, with the Reynolds number ranging from 3.2×10^4 to 7.4×10^4. An experimental investigation of the flow around two fixed side-by-side cylinders at Re = 2.5×10^4 is conducted in [7]. A high Reynolds number of Re = 1.1×10^5 is investigated experimentally in [8], focused on interference between two tandem cylinders while the spacing in between them is increased up to 10 diameters. In the latter study, the reattachment of the flow separated from the upstream cylinder to the downstream cylinder occurs at the spacing range of $3 < L/D < 4$. A numerical study on a three-dimensional flow over two tandem cylinders at Re = 2.2×10^4 is performed in [9], with the analysis of the interference effect and the vortex interaction of two tandem cylinders at the spacing from 2D to 4D. An experimental investigation in [10] also considers a large Reynolds number spanning from 2×10^5 to 6×10^6 for the cylinders' centre-to-centre spacing of 1.56, and the influence of the incidence angle on flow-induced vibrations characteristics is studied. Overall, research on the vortex formation under conditions of a high Reynolds number flow over diverse arrangements of multiple structures still appears to be limited.

Sets of three and four rigid and flexible structures in proximity to each other are studied experimentally and numerically in the following works. In [11], the force coefficients and vortex formation patterns of three identical stationary circular cylinders placed in three different positions relative to a squared cylinder are modelled numerically in the uniform and sheared flow. Here, a higher mean drag is observed in uniform current conditions. Experimental studies of the dynamics of three and four flexible cylinders in a tandem arrangement are performed in [12]. A three-dimensional wake transition in the flow over four squared cylinders at low Reynolds numbers is investigated in [13]. In [14], three and four long flexible cylinders undergoing FIV are considered when the structures are in an initial side-by-side configuration. Further numerical studies for three and four structures are performed in [15–19], and a distinct set of circular structures in a triangle is investigated in [20].

A more advanced set of five cylinders arranged in a circle is considered in [21]. The use of small control cylinders (two, four and eight) placed around the main cylinder for the purpose of mitigating the fluid loads is studied in [22,23], and a similar idea of using a group of equally spaced flexible shrouds in the form of a mesh to suppress the fluid forces and vortex-induced vibrations (VIV) is explored in [24]. More advanced geometries for the suppression of hydrodynamic loads, such as in [25], can be offered related to this experience. The 2D numerical simulation of the flow past six identical circular cylinders at a low Reynolds number of 100 is performed in [26], including studying the effect of the spacing ratio, pressure distribution and Strouhal number. The literature review, in general, reveals that there is a limited number of studies considering flow effects for sets exceeding four structures.

Another branch of studies considers advanced case geometry and, for instance, investigates a single rotating structure of varying cross-sectional geometry, as performed in [27]. Cylinders of different sizes in tandem are considered in [28,29]. The mitigation of hydrodynamic loads using changes to the cross-sectional geometry is critically evaluated in [30] for the D-shape option, and an advantageous force reduction is reported. Alternative cylinder shapes of a 3D wavy type with the associated flow effects are proposed in [31] for the purposes of wake suppression.

Studies on slender structures immersed in a sheared flow develop reduced-order models [32] and numerical schemes [33] to investigate the separation of the boundary layer [34] and effects associated with the specific range of the Reynolds number, characterizing the flow profile [35–37].

Analysis of available studies indicates an existing gap in the studies considering: (i) multiple structures; (ii) the critical flow regime; (iii) different cross-sectional shapes; (iv) non-uniform flows. The present research is designed to fill this gap for an arrangement of six structures. The cylinders are assumed identical and are placed in a 2 × 3 matrix configuration under both uniform, and planar sheared flow at the averaged Reynolds number of the flow profile of 2.5×10^5. The effect of changes in the cross-sectional geometry to the D shape is analyzed through the lens of alternative flow velocity profiles. Simulations are performed with the computational fluid dynamics (CFD) method using ANSYS Fluent software capabilities, following the research [38], including the initial benchmarking of the simulation with published results for submerged cylindrical objects.

This paper consists of the following sections. Section 1 provides a brief theoretical background on the topic. Section 2 gives an overview of the numerical method, model verification, and case matrix. Section 3 discusses the results of this study, and Section 4 provides conclusions for this work.

2. Numerical Model

A system of six identical cylinders in a 2 × 3 matrix configuration is considered in this research, as shown in Figure 1, and the cylinders are numbered in Figure 1a for the convenience of discussing the results. The study investigates three different geometrical shapes, namely, shape 1 (circular cylinders), as in Figure 1a, shape 2 (D-shape with the circular side facing the flow), as in Figure 1c, and shape 3 (D-shape with the flat side facing the flow), as in Figure 1d. The cylinder diameter is D = 0.5 m. The CFD simulations are performed for the computational domain with a size of 60D × 32D. The distance from the inlet to the centres of upstream cylinders is 10D, and the distance from the outlet boundary is 50D. The two lateral boundaries are located at a distance of 14D away from the centres of the top and bottom cylinders, respectively. The top and bottom cylinders are separated by a constant vertical distance of 4D. This distance does not change for all simulations in this work. The incoming flow enters the domain from the inlet, and periodic and shadow conditions are used as the top and bottom boundary. At the outlet boundary, the value of gauge pressure is set to zero.

The study is designed to report two sets of results. The first set of results is obtained from parametric studies for the first cross-sectional shape only—identical circular cylinders. Here, the distances L/D among the structures in a row are varied simultaneously from 2 to 7, while the distance between the rows remains fixed to 4D. Two velocity profiles are considered: the uniform current, shown in Figure 1a, and the linearly sheared current, in Figure 1b. The planar sheared flow is defined by the linear velocity profile $U(y)$, depending on the vertical inlet coordinate y. The averaged velocity at $y = 0$ is $U_c = 0.5$ ms^{-1}, which is consistent with the Reynolds number of 2.5×10^5 at the centreline of the computational domain, or:

$$U(y) = U_c - By \quad (1)$$

where B = 0.022 c^{-1} is the gradient of the velocity profile so that the maximum velocity U_{max} = 0.676 ms^{-1} of the profile is at the bottom boundary of the domain.

In the second set of results, the data for both uniform and sheared flows are compared for all three cross-sectional shapes, while the structures are placed in a row at exactly the same distance of L/D = 2, and the distance between the rows, again, remains fixed to 4D.

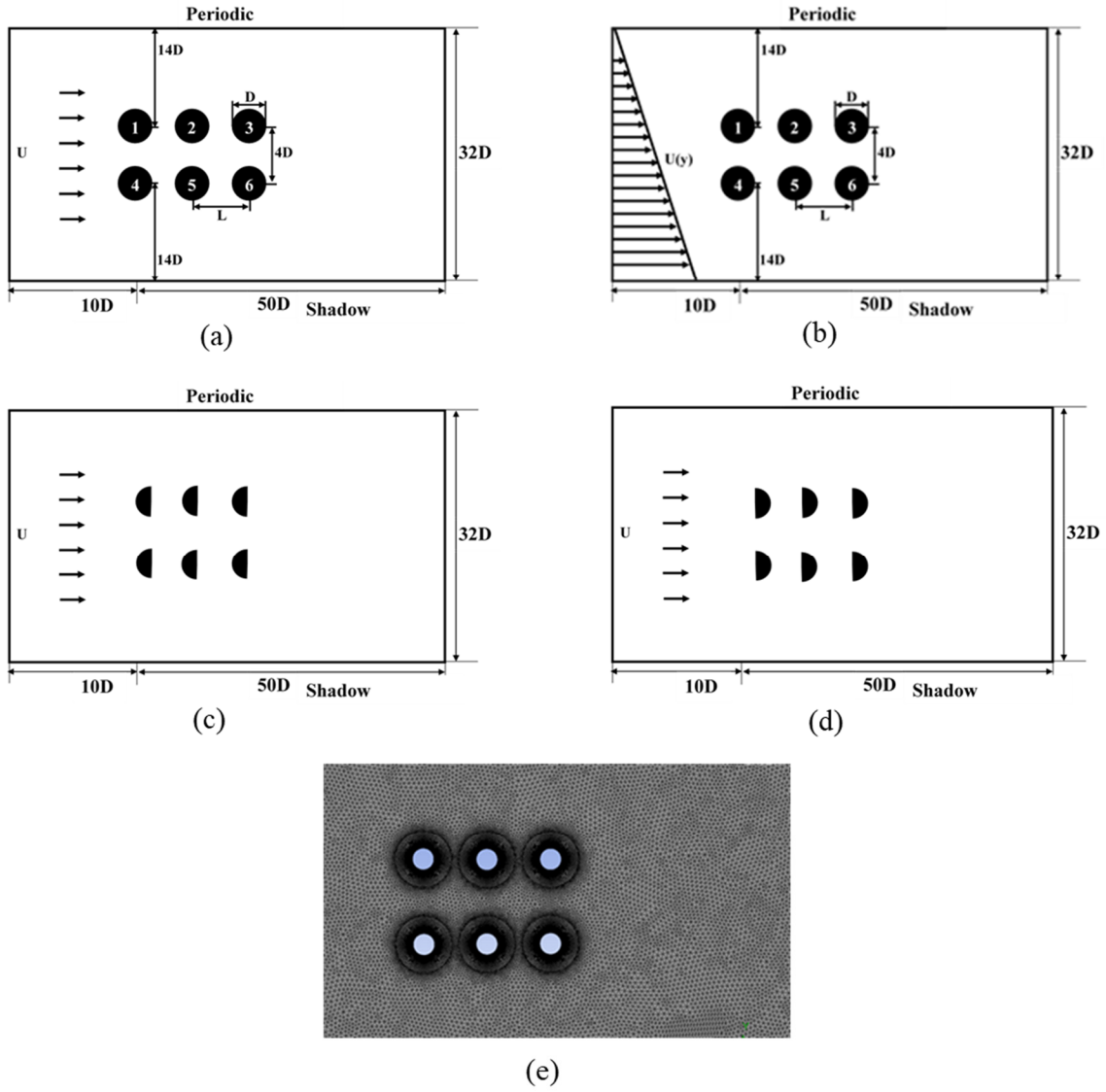

Figure 1. General view on the computational domain: (**a**) shape 1 cylinder immersed in the uniform flow; (**b**) shape 1 cylinder immersed in the linearly sheared flow; (**c**) shape 2 cylinders immersed in the uniform flow; (**d**) shape 3 cylinders immersed in a uniform flow; (**e**) mesh of the computational domain.

The flow around cylinders is modelled using the transient, incompressible 2D Navier–Stokes equation, DES solver, with k–ω SST as the turbulence model, PISO algorithm and the time step of 0.01 s. The DES method uses both Reynolds-Averaged Navier-Stokes (RANS) and Large Eddy Simulation (LES) approaches [39]. The continuity and momentum equation of RANS for incompressible flow are as follows:

$$\frac{\partial(\rho\overline{u_i})}{\partial x_i} = 0, \tag{2}$$

$$\frac{\partial(\rho\overline{u_i})}{\partial t} + \frac{\partial}{\partial x_j}\left(\rho\overline{u_i u_j} + \rho\overline{u_i' u_j'}\right) = \frac{\partial\overline{p}}{\partial x_i} + \frac{\partial\overline{\tau_{ij}}}{\partial x_j}, \tag{3}$$

where p is the mean pressure, $\overline{u_i}$ means the average Cartesian components of the velocity vector, $\rho\overline{u_i'u_j'}$ are the Reynolds stresses, ρ is the density of the fluid, and $\overline{\tau_{ij}}$ is the mean viscous stress vector components, as follows:

$$\overline{\tau_{ij}} = \mu\left(\frac{\partial\overline{u_i}}{\partial x_j} + \frac{\partial\overline{u_j}}{\partial x_i}\right), \tag{4}$$

where μ denotes the dynamic viscosity. The Large Eddy Simulation (LES) is a spatially filtered Navier-Stokes equation [39], and for the incompressible flow they are shown in Equations (5) and (6):

$$\frac{\partial\overline{u_i}}{\partial x_i} = 0, \tag{5}$$

$$\frac{\partial(\overline{u_i})}{\partial t} + \frac{\partial}{\partial x_j}(u_i u_j) = -\frac{1}{\rho}\frac{\partial\overline{p}}{\partial x_i} + v\frac{\partial^2\overline{u_i}}{\partial x_j\partial x_j} - \frac{\partial\overline{\tau_{ij}}}{\partial x_j}, \tag{6}$$

where $\overline{u_i}$ and $\overline{p}$ represent the resolved filtered velocity and pressure, respectively.

The diffusion term of the DES model is given by

$$Y_k = \rho\beta^* k\omega F_{DES}, \tag{7}$$

where β^* is the constant of the SST model, k denotes fluctuation of the turbulent kinetic energy, ω is the specific energy dissipation rate, and F_{DES} is expressed as

$$F_{DES} = \max\left(\frac{L_t}{C_{des}\Delta_{max}}, 1\right), \tag{8}$$

where C_{des} is a calibration constant used in the DES model with a value of 0.61, Δ_{max} is the local maximum grid map $\Delta = (\Delta_1,\ \Delta_2,\ \Delta_3)^{\frac{1}{3}}$. The turbulent length scale L_t is:

$$L_t = \frac{\sqrt{k}}{\beta^*\omega} \tag{9}$$

The DES-SST model also offers the option to protect the boundary layer from the limiter (delayed option). This is achieved with the help of the zonal formulation of the SST model:

$$F_{DES} = \max\left(\frac{L_t}{C_{des}\Delta_{max}}(1 - F_{SST}), 1\right), \tag{10}$$

where F_{SST} = 0, F_1, F_2, and F_1, F_2 are the mixed functions of the SST model.

The mesh independence test results are reported in Table 1 for the uniform flow of the Reynolds number of 2.5×10^5, and the mesh, shown in Figure 1e, is selected for all calculations in the next section. For this mesh of the numerical model, the edges of the cylinders are given 96 radial divisions. Mapped face meshing and biasing with a high bias factor are used in order to significantly increase the number of elements located close to the cylinder and provide a fine resolution in this area. The thickness of the first layer of mesh Δy is set to 0.01D. The obtained results for the mesh independence test in the present work agree well with the published data, especially from experiments, as shown in Table 1. Based on these data, the results obtained using Mesh 2 are reported in Section 3, and they include fluid force coefficients, their signals and frequencies, and also vortex shedding features. The total drag force coefficient C_D acting on the cylinder is given as the sum of the mean drag coefficient C_{D0} and the fluctuating drag coefficient $C_D{}^{fl}$:

$$C_D = C_{D0} + C_D^{fl} \tag{11}$$

Table 1. Mesh independence test results, compared to [26,40–44].

Re = 2.5 × 10^5			
Cases	C_{D0}	**Number of Cells**	**Strouhal Number**
Current Study			
Mesh 1	0.99	60,133	0.24
Mesh 2	1.09	85,227	0.24
Mesh 3	1.09	122,091	0.24
Published data			
Lehmkuhl et al. (2014) (LES) [40]	0.833	-	0.238
Achenbach&Heinecke (1981) (Experiment) [41]	1.135	-	0.23
Schewe (1983) (Experiment) [42]	1.120	-	0.20
Re = 100			
Current study	1.41	85,227	0.183
Gao et al. (2020) [26]	1.375	28,100	0.166
Re = 3.6 × 10^6			
Current study	0.45	85,227	
Porteous et al. (2015) [43]	0.4206	-	
Nazvanova et al. (2022) [44]	0.4657	74,496	

3. Results and Discussion

3.1. Variation of Distances among Circular Cylinders in Uniform and Sheared Flows

The first set of results for the mean drag coefficient C_{D0}, fluctuating drag coefficient $C_D{}^{fl}$ and lift coefficient C_L for six cylinders are summarized in Table 2. All these data correspond to the shape 1 (circular) structures only, and the L/D ratio varies from 2 to 7, as in column 1. The data are reported for each structure, marked C1 to C6 in the table heading, in accordance with the numbers of cylinders in Figure 1a. Table 2 contains two sections for the results obtained for the uniform flow and sheared flow simulations.

Results for the fluctuations of hydrodynamic force coefficients for the first structure C1 for the considered L/D ratios in comparison are presented in Figure 2, and results for the remaining five structures are given in Appendix A, Figures A1–A5. These figures each include the signal of the fluctuating drag coefficient, lift coefficient, and frequency spectra of both coefficient signals in comparison. It is possible to see from Table 2 and the figures that, at L/D = 3, the majority of cylinders experience the least mean drag. At the same time, the highest fluctuating drag is observed for the majority of structures at L/D = 2. The upstream cylinders C1 and C4 experience, on average, a higher mean drag force compared to that of the mid- and downstream cylinders, which is related to the immersion of the mid- and downstream cylinders in the wake of the upstream cylinders. This agrees well with the work [12]. The midstream cylinders experience the least mean drag coefficient. Unusual mean drag coefficient values with an increasing spacing ratio are observed for cylinder 5. The downstream cylinders are in the wake region of the frontal cylinders, and the shielding effects are observed in the flow patterns around them. Downstream cylinders achieve the maximum mean drag coefficient of 0.41 at L/D = 2.

Table 2. Hydrodynamic force coefficients were obtained in the first series of simulations for the structures with the first cross-sectional shape.

L/D	C1			C2			C3			C4			C5			C6		
	Uniform Flow																	
	C_{D0}	C_D^{fl}	C_L	C_{D0}	C_D^{fl}	C_L	C_{D0}	C_D^{fl}	C_L	C_{D0}	C_D^{fl}	C_L	C_{D0}	C_D^{fl}	C_L	C_{D0}	C_D^{fl}	C_L
2	0.7	0.31	0.90	0.28	1.12	1.2	0.41	1.29	1.5	0.64	0.32	0.89	0.21	0.89	1.1	0.41	1.14	1.2
3	0.51	0.18	0.84	0.14	0.71	1.5	0.17	0.56	1.1	0.51	0.20	0.84	0.19	1.0	1.4	0.13	0.70	1.3
4	0.5	0.17	0.76	0.2	0.55	1.5	0.2	0.8	1.4	0.5	0.18	0.68	0.18	0.60	1.3	0.18	0.30	1.1
5	0.53	0.18	0.8	0.19	0.39	1.0	0.28	0.64	0.9	0.5	0.17	0.72	0.23	0.65	1.3	0.28	0.66	1.3
6	0.54	0.17	0.79	0.23	0.47	1.2	0.3	0.60	1.0	0.53	0.18	0.76	0.2	0.50	1.2	0.31	0.69	1.2
7	0.50	0.17	0.63	0.24	0.48	1.0	0.31	0.80	1.4	0.51	0.19	0.76	0.26	0.41	1.2	0.28	0.65	1.2
	Planar Sheared Flow																	
2	0.43	0.23	0.76	0.28	1.0	1.42	0.29	1.34	1.57	0.49	0.19	0.8	0.29	0.90	1.28	0.28	0.94	1.4
3	0.47	0.19	0.77	0.15	0.60	1.34	0.18	0.50	1.5	0.55	0.18	0.9	0.16	1.0	1.64	0.13	0.38	1.0
4	0.47	0.18	0.71	0.21	0.50	1.29	0.22	0.68	1.33	0.52	0.19	0.76	0.19	0.60	1.31	0.18	0.46	0.9
5	0.49	0.15	0.8	0.16	0.29	1.15	0.23	0.60	0.73	0.53	0.19	0.78	0.24	0.50	1.48	0.31	0.56	1.1
6	0.50	0.15	0.75	0.25	0.50	1.18	0.30	0.63	1.03	0.55	0.19	0.89	0.21	0.41	1.20	0.32	0.73	1.2
7	0.47	0.15	0.66	0.27	0.43	1.18	0.26	0.74	1.03	0.55	0.19	0.82	0.25	0.42	1.32	0.29	0.63	1.1

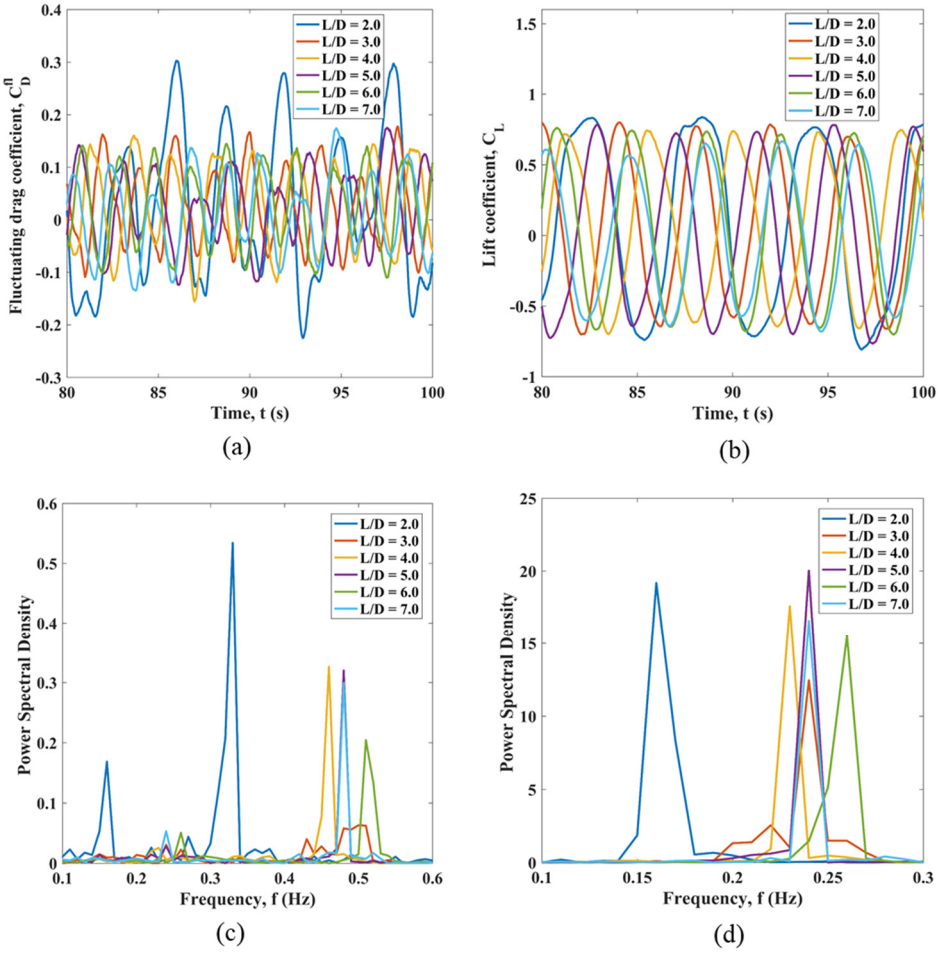

Figure 2. Fluid force coefficients for cylinder 1 immersed in the uniform flow: (**a**) time history of the fluctuating drag coefficient; (**b**) time history of the lift coefficient; (**c**) the fluctuating drag coefficient FFT; (**d**) the lift coefficient FFT.

The fluctuating drag coefficient of the cylinders varies significantly with L/D, and the downstream cylinders experience the highest fluctuating drag coefficient. A decrease in the fluctuating drag coefficient is observed for cylinders 1, 2, 3, 4 and 6 as the L/D increases from 2 to 4, with the maximum fluctuating drag coefficient of 1.07 for cylinder 5 occurring at L/D = 3.

Increasing L/D from 2 to 4 decreases the maximum amplitude of the lift coefficient signals of the upstream cylinders in the uniform flow. The midstream cylinders experience the maximum amplitude of lift coefficient signals, and the downstream cylinders—have the least amplitude. A constant frequency of 0.3 Hz and 0.16 Hz of the drag and lift coefficient signals, respectively, is observed for all cylinders at L/D = 2.0. Very low frequencies of the fluctuating drag coefficient signal are found for downstream cylinders in general. The upstream cylinders demonstrate the highest frequencies of the fluctuating drag coefficient signal. The Fast Fourier Transform (FFT) data of the lift coefficient signal show a single dominating peak for the upstream cylinders in the uniform flow. Multiple frequencies are found in the fluctuating drag coefficient signals at L/D = 2. The fluctuating drag coefficient signal has a frequency which is twice the frequency of the lift coefficient signal of the upstream and midstream cylinders, while slightly different values are observed for the downstream structures. The observation of the more regular force signal for the upstream structures and the more irregular nature of forces acting on other cylinders agrees with the works [10,44]. The irregular nature of fluid forces is likely related to the reattachment of shear layers separated from the frontal cylinders and the impingement of the vortex shedding in the reattachment flow regime. The effect of L/D on the drag and lift force of the upstream cylinders is small.

Results of simulations for the planar sheared flow are summarized in Table 2, Figure 3 and Appendix B. For the planar sheared flow, the maximum mean drag coefficient of 0.55 is observed for the upstream cylinder 4. The upstream cylinders experience higher mean drag coefficients compared to the mid- and downstream cylinders, similar to the uniform flow. At L/D = 3, the upstream cylinders experience an increase in the mean drag coefficient, which is opposite to the uniform flow. The least mean drag coefficient of the mid- and downstream cylinders occurs at L/D = 3. The upstream cylinder 1 shows an increasing mean drag coefficient with the increasing spacing ratio from 2 to 6. Relatively close values of the fluctuating drag coefficient are observed for the upstream cylinders with the increasing spacing ratio. The maximum fluctuating drag coefficient for all structures in the linearly sheared flow is found at L/D = 2. The lift coefficient amplitude is higher for the mid- and downstream cylinders than for the upstream structures. The effect of L/D on the drag and lift force of the upstream cylinders appears to be small.

As shown in Figure 3 and Appendix B, signals of the fluctuating drag and lift coefficient of the upstream cylinders appear to have a relatively regular time history. Competing frequencies are observed, mainly in the hydrodynamic forces acting on the mid- and downstream cylinders. The maximum frequency of 0.5 Hz of the fluctuating drag coefficient signal is found for the upstream cylinder 4. Downstream cylinders show the lowest frequency of the fluctuating drag coefficient signal. At the same time, upstream cylinder 4 and midstream cylinder 5 demonstrate the maximum frequency values of the fluctuating drag coefficient signal. The frequency of the lift coefficient signal shows less variation with increasing spacing ratios than the fluctuating drag force coefficient. The bottom row of cylinders shows higher frequencies of the lift coefficient signal than the top row of cylinders. The upstream cylinder 4 and the midstream cylinder 5 show close values of the lift coefficient frequency. The FFT data for the fluctuating drag coefficient signal show two dominant peaks for the top cylinders in the planar sheared flow. The drag coefficient signal oscillates at a frequency which is twice the lift coefficient signal of the upstream cylinders and midstream cylinder 5. The fluctuating drag coefficient signal of midstream cylinder 2 and downstream cylinder 3 has a frequency which is similar to the lift coefficient signal.

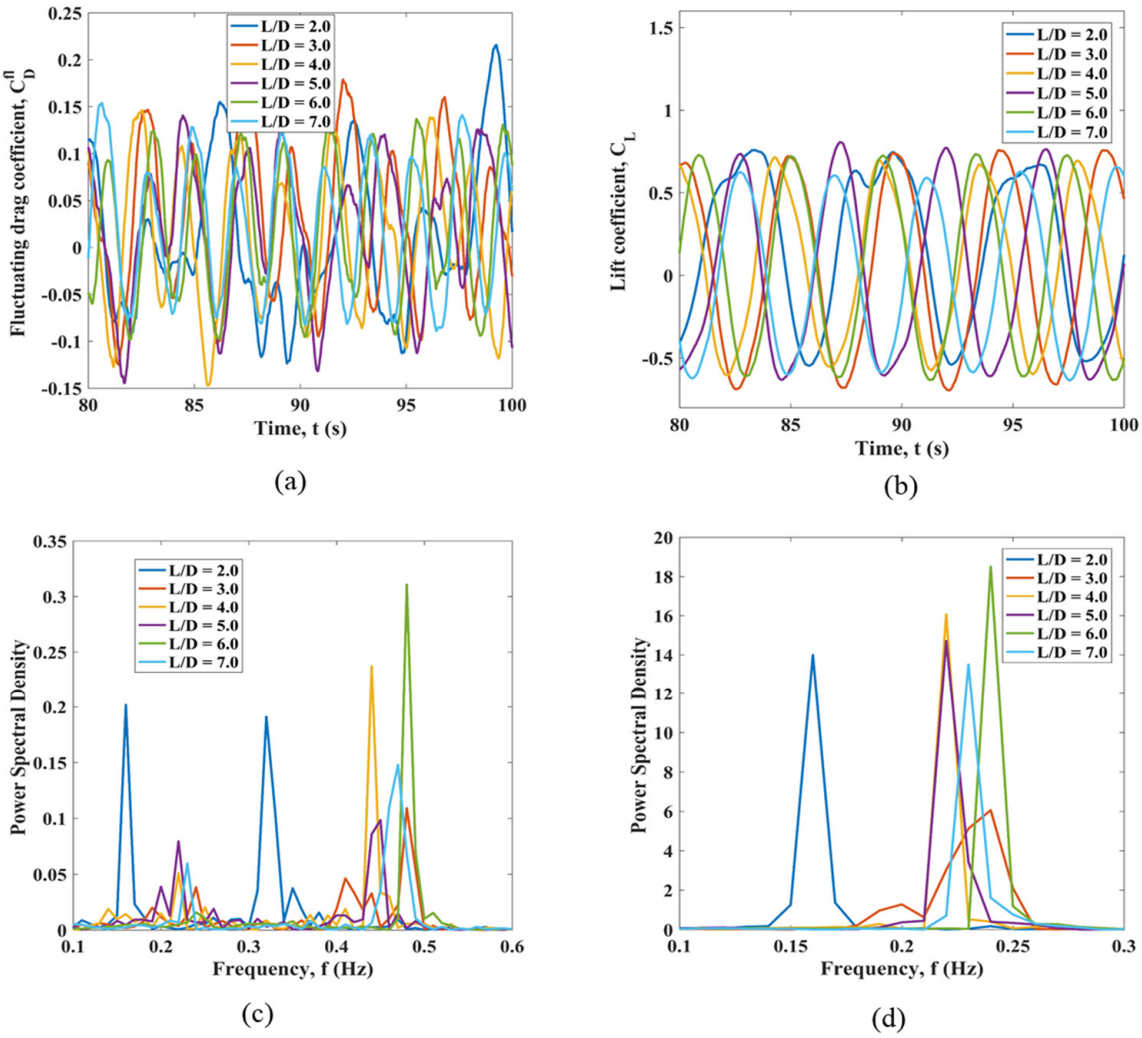

Figure 3. Fluid force coefficients for cylinder 1 immersed in planar sheared flow: (**a**) time history of the fluctuating drag coefficient; (**b**) time history of the lift coefficient; (**c**) the fluctuating drag coeffi–cient FFT; (**d**) the lift coefficient FFT.

3.2. Effect of the Cross-Sectional Shape on Hydrodynamic Loads

The second set of simulations is performed for three cross-sectional shapes (circular and two D-shapes), while cylinders are placed at the distance of L/D = 2 in a row and subjected to the uniform and planar sheared flow. The mean drag coefficients demonstrate quite substantial changes among the considered cross-sectional shapes and are shown in comparison in Table 3. Here, the upstream cylinders C1 and C4 with the shape 3 cross-section experience the highest mean drag force in both the uniform and linearly sheared flow. The upstream cylinders with shape 2 of the cross-section reduce the mean drag coefficient substantially for the mid- (C2 and C5) and downstream (C3 and C6) cylinders. The downstream cylinders with the cross-sectional shape 3 demonstrate a notably higher mean drag coefficient compared to the downstream cylinders with the cross-sectional shape 1 and shape 2.

Table 3. Mean drag coefficients for six structures in a group for three cross-sectional shapes and two types of currents.

Flow Types	Mean Drag Coefficient, C_{D0}					
	C1	C2	C3	C4	C5	C6
	Shape 1					
Uniform	0.7	0.28	0.41	0.64	0.21	0.41
Planar sheared	0.43	0.28	0.29	0.49	0.29	0.28
	Shape 2					
Uniform	0.86	0.0034	0.028	0.88	0.02	0.17
Planar sheared	0.82	−0.015	0.035	0.97	−0.017	0.18
	Shape 3					
Uniform	1.45	0.14	0.52	1.44	0.08	0.66
Planar sheared	1.31	0.2	0.73	1.54	0.14	0.55

Figure 4 and Appendix C show time histories of the hydrodynamic coefficients and the corresponding FFT data for six structures with three considered geometrical shapes under the uniform flow at L/D = 2. Here, the fluctuating drag and lift coefficient signals of the shape 2 cylinders appear more stable and have lower amplitudes than those for the shape 1 and shape 3 cylinders. The fluctuating drag and lift coefficients signals seem very unstable for the shape 3 cylinders. Several dominating peaks are present in the fluctuating drag coefficient signals of the shape 3 cylinders, and a single peak of the dominant frequency is found in the power spectrum density (PSD) of the lift coefficient signals. Moreover, it is possible to note that the hydrodynamic coefficient signals for the cylinders with the third cross-sectional shape have low frequencies in general. The maximum frequencies of the hydrodynamic coefficient signals are observed for the shape 2 cylinders. This, combined with the overall lower amplitudes of the signals and the relatively reduced mean drag coefficient values, allows stating that the cross-sectional shape 2, especially for the mid- and downstream structures provides the suppression effect of hydrodynamic loads. This result is quite consistent with the data reported in [30].

Figure 5 and Appendix D show time histories of the hydrodynamic coefficients and the corresponding FFT data for the six cylinders of three geometrical shapes in the planar sheared flow at L/D = 2. Here, similar to the results obtained for the uniform flow, structures with the shape 2 cross-section demonstrate more stable signals of fluid force coefficients, with relatively lower amplitudes than for shapes 1 and 3, and the maximum frequency among the considered signals.

The shape 3 used for the cross-section of structures leads to several dominant frequencies in the fluctuating drag coefficient signals and a single dominant peak in the PSD of the lift coefficient signals for all cylinders. Similar to the effects observed in the uniform flow for this arrangement, the cross-sectional shape 3 leads to the low-frequency fluctuations of the lift and drag forces.

Figures 6 and 7 show the vorticity contours for the flow around six cylinders at L/D = 2 for three considered geometrical shapes of the cross-section in the uniform and planar sheared flow, respectively. Here, the shape 1 cylinder allows observing the reattachment regime for both flow types, where shear layers are shed from the upstream cylinders and reattached to the face of the midstream cylinders. Subsequently, shear layers shed from the midstream cylinders reattach to the face of the downstream cylinders, and the vortex shedding is observed only in the wake of the downstream cylinders. It is possible to observe two vortex streets of the type close to P+S formed behind the downstream cylinders, and these vortex streets merge later in the process, at some distance past the group of cylinders, in a single large wake.

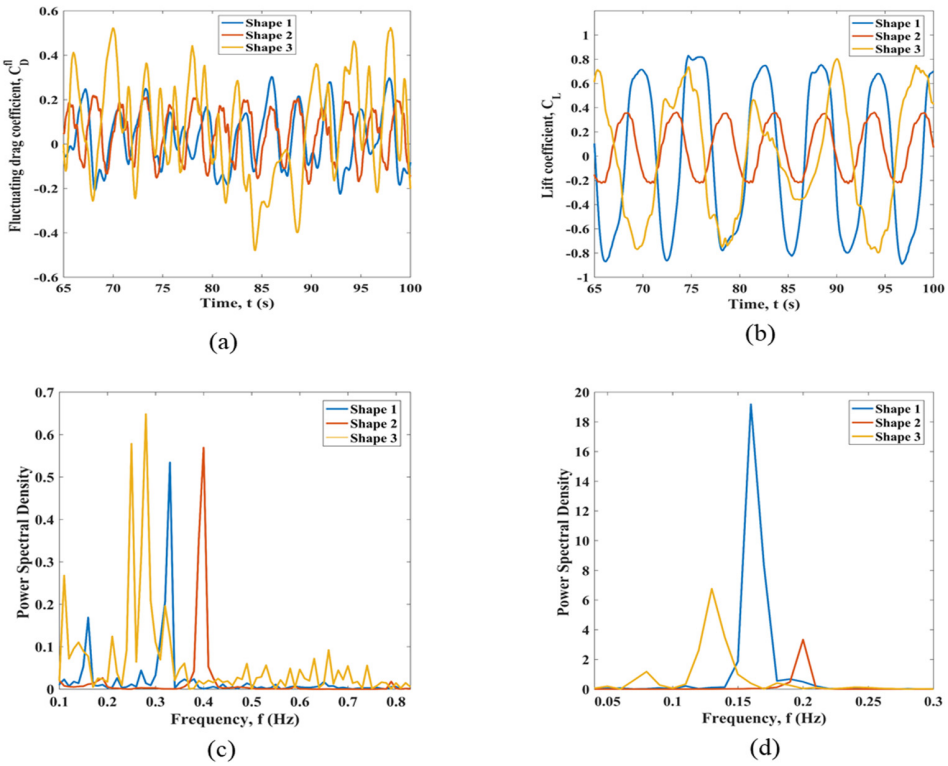

Figure 4. Fluid force coefficients for cylinder 1 immersed in uniform flow: (**a**) time history of the fluctuating drag coefficient; (**b**) time history of the lift coefficient; (**c**) the fluctuating drag coefficient FFT; (**d**) the lift coefficient FFT.

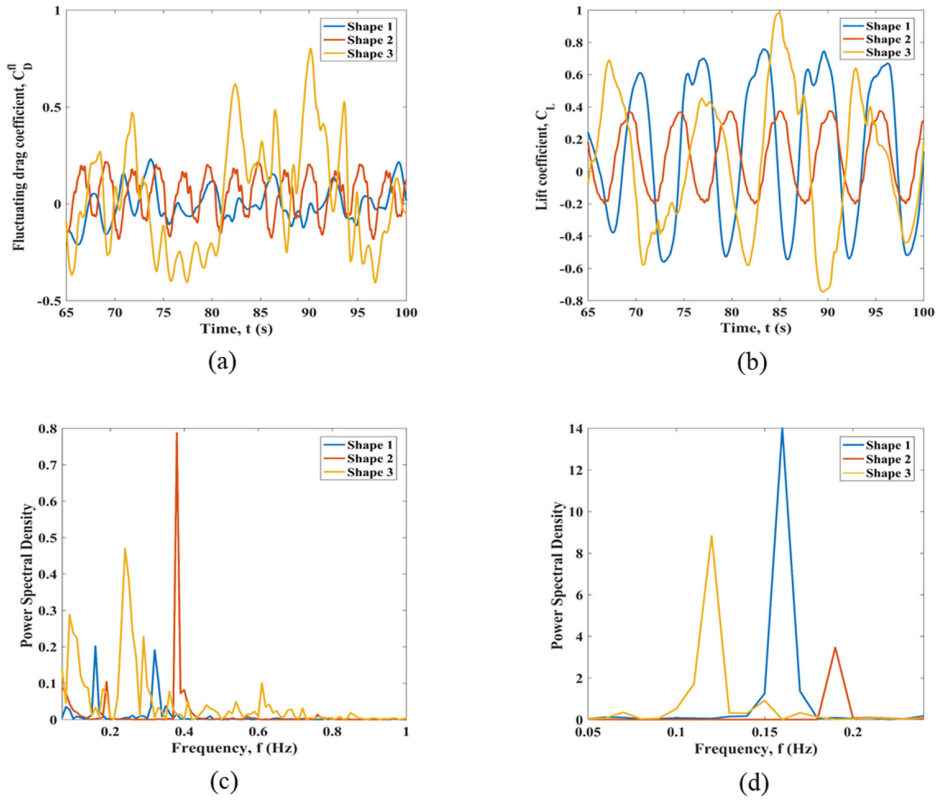

Figure 5. Fluid force coefficients for cylinder 1 immersed in planar sheared flow: (**a**) time history of the fluctuating drag coefficient; (**b**) time history of the lift coefficient; (**c**) the fluctuating drag coefficient FFT; (**d**) the lift coefficient FFT.

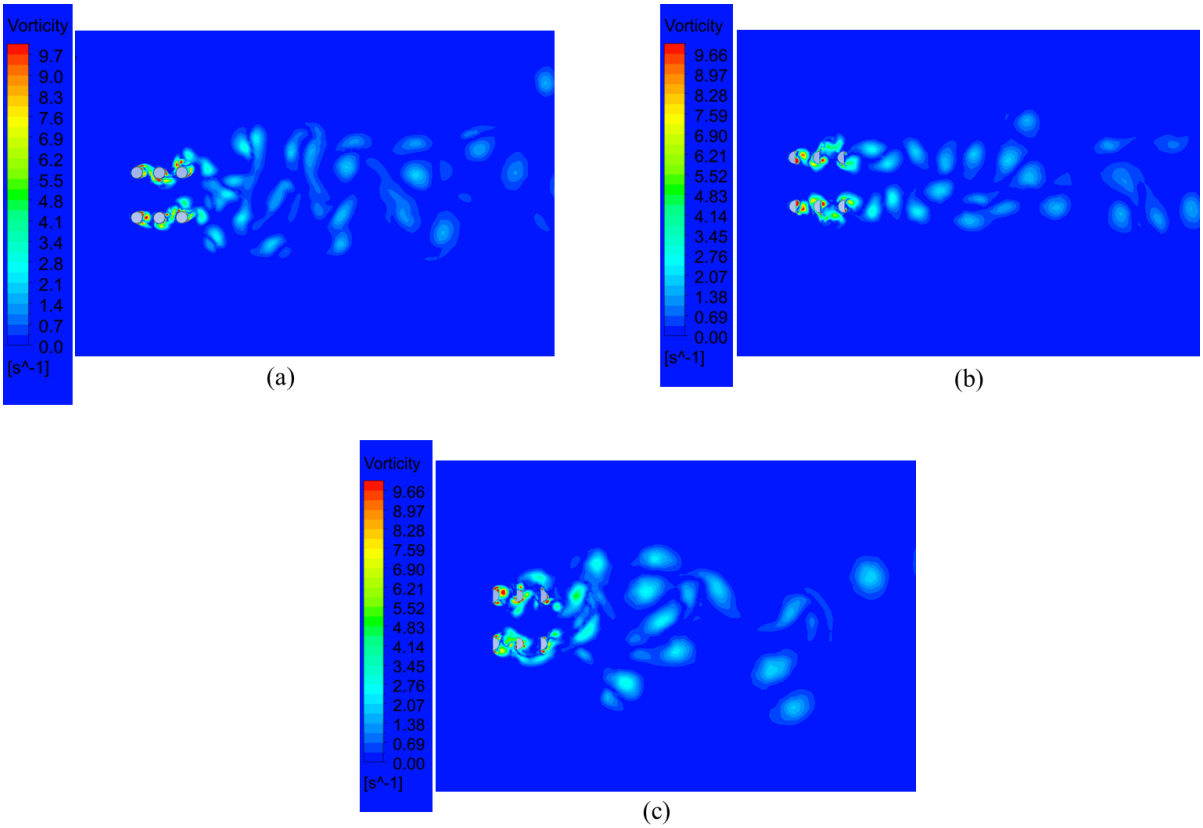

Figure 6. Vorticity contours for the uniform flow simulations at L/D = 2 for the cylinder of a variative cross-section: (**a**) Shape 1; (**b**) Shape 2; (**c**) Shape 3.

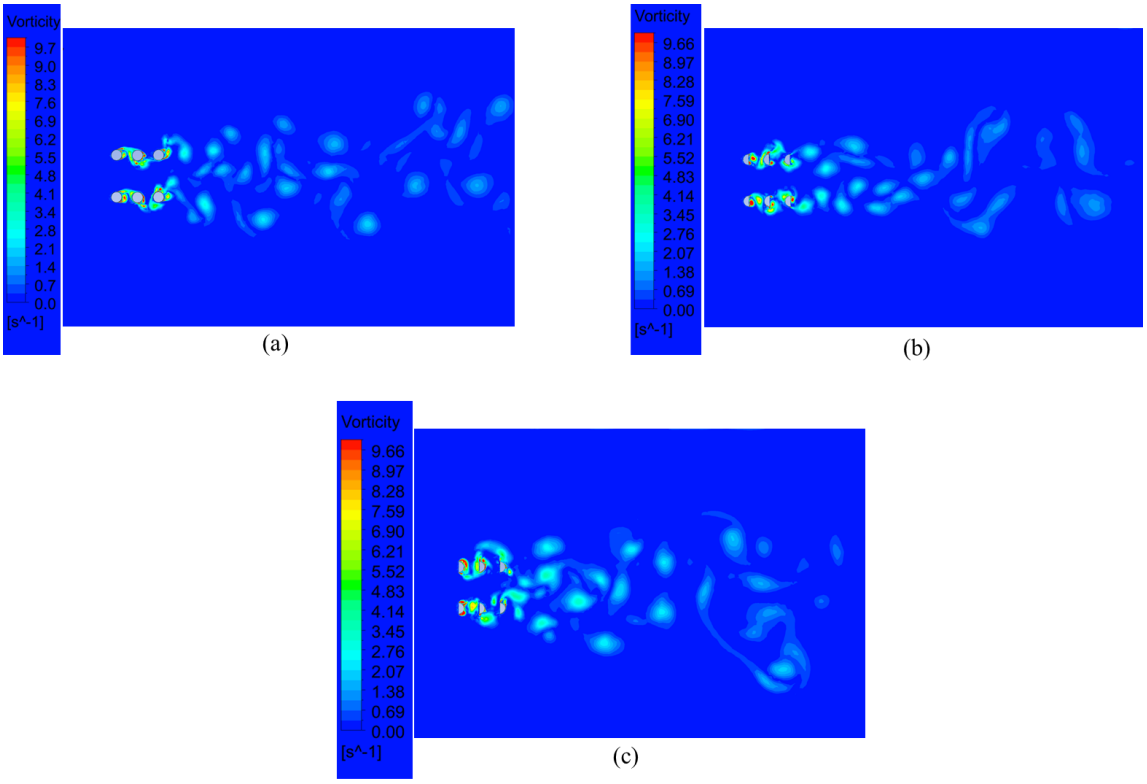

Figure 7. Vorticity contours for the linearly sheared flow simulations at L/D = 2 for the cylinder of a variative cross-section: (**a**) Shape 1; (**b**) Shape 2; (**c**) Shape 3.

Shape 2 structures in Figure 6b result in substantially narrower vortex streets than for shape 1 in Figure 6a, and more regular vortex streets, than for shape 3 in Figure 6c. For the shape 2 cylinders, the top shear layer of the upstream cylinder 1 attaches to the lower side of the midstream cylinder 2, and the lower shear layer of the upstream cylinder 4 attaches to the top side of the midstream cylinder 5. The downstream cylinders of shape 2 in Figure 6b produce two almost parallel vortex streets of a type close to 2S and a little expansion in space past the group of structures so that the vortex streets interfere with each other significantly later than the vortex streets in Figure 6a,c. These features of the vortex street for the shape 2 structures appear to be similar for both uniform flow in Figure 6b and sheared flow in Figure 7b.

The downstream cylinders of shape 3 in both Figures 6c and 7c demonstrate the flow dynamics of the shear layers' reattachment in a way similar to shape 2. However, the wakes show a relatively faster expansion behind the structures. The downstream cylinders of shape 3 produce two vortex streets of a type close to 2P, which merge quickly into a single fast-expanding vortex street comprising single vortices. Based on the comparison of vortex streets behind the structures in a matrix configuration, the second cross-sectional shape can be considered advantageous due to its ability to reduce and order the vortex formation process.

4. Conclusions

The present study investigates the flow around six identical cylinders of three distinct geometrical shapes in a 2×3 matrix configuration using the computational fluid dynamics model. The work considers the critical flow regime at the averaged Reynolds number of 2.5×10^5 for both uniform and linearly sheared velocity profiles. The study presents fluid force coefficients and characteristics of their signals, discusses the vortex formation around structures, and demonstrates the effects of the variation of the spacing ratio. Two sets of results are generated: for the circular cylinder shapes only, while the L/D ratio varies from 2 to 7, and for the fixed spacing ratio L/D = 2 among the structures, while three cross-sectional shapes are tested.

The results indicate that the mean drag coefficient for the upstream cylinders is always higher than that of the midstream and downstream cylinders for all considered spacing ratios. In the second set of simulations, at L/D = 2, the upstream cylinder 4 of shape 3 (D-shape with the flat side facing the flow) has the highest mean drag coefficient when subjected to the planar sheared flow. For both flow profiles, shape 3 leads to the multi-frequency complex signals of the fluctuating drag coefficient, while a single-frequency signal is indicated for the lift coefficient. Simulations with this shape also demonstrate a fast-expanding, near-chaotic vortex formation process behind the group of structures.

Simulations with cylinders of shape 2 (D-shape with the circular side facing the flow) demonstrate the reduction of the mean drag coefficient on the midstream and downstream cylinders. At L/D = 2, the shape 2 cylinders lead to the highest frequency of the hydrodynamic coefficient signals and visibly reduced amplitudes. Complex vortex formation is observed, with the dominant vortex street type of 2S and relatively clear vortex structures in general, with a less pronounced expansion across the fluid domain.

Based on the performed analysis, shape 2 (D-shape with the circular side facing the flow) can be recommended to reduce the hydrodynamic loads on the midstream and downstream structures in a submerged array. Investigations in this direction may be continued in the future by expanding the range of Reynolds numbers, considering complex 3D flows, and staggered arrangements of more than 6 structures.

Author Contributions: Conceptualization, methodology, validation, investigation, data curation, writing—original draft preparation, writing—review and editing, H.F.A.; conceptualization, methodology, writing—review and editing, supervision, funding acquisition, V.K. All authors have read and agreed to the published version of the manuscript.

Funding: The authors would like to acknowledge the support of the National Project "Science and Universities" of the Ministry of Science and Higher Education of the Russian Federation, grant number FEWN-2021-0012.

Institutional Review Board Statement: Not applicable.

Informed Consent Statement: Not applicable.

Data Availability Statement: The research data are available upon e-mail request.

Conflicts of Interest: The authors declare no conflict of interest.

Appendix A. Parametric Study for the L/D Variation for Circular Cylinders in Uniform Flow

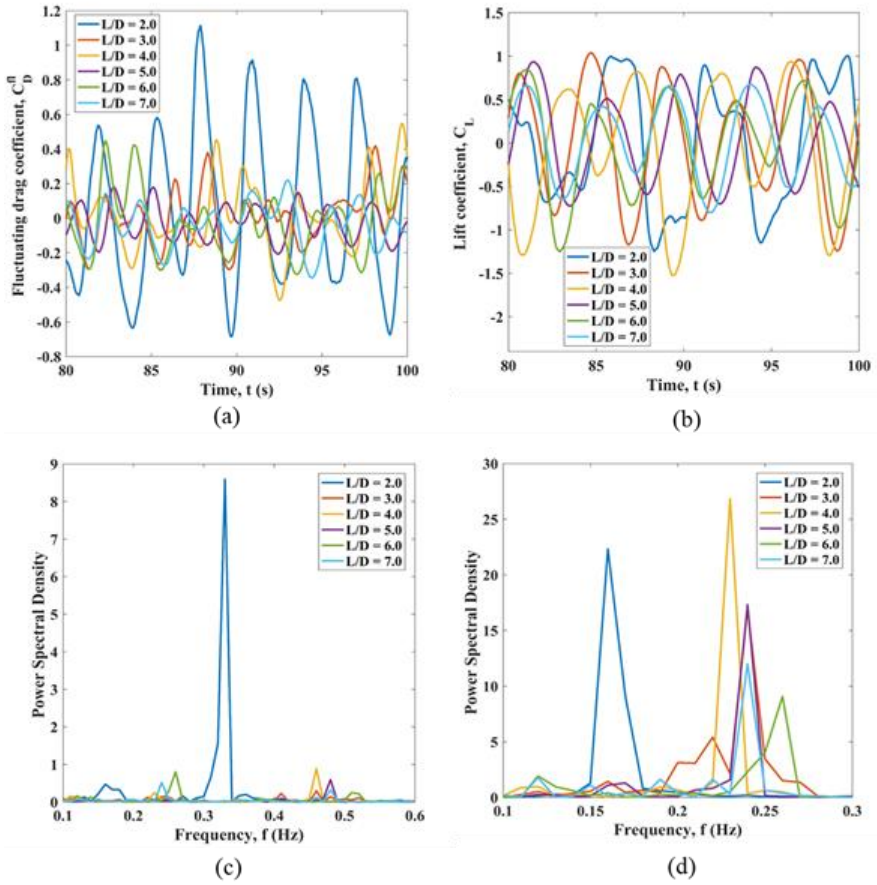

Figure A1. Fluid force coefficients for cylinder 2 immersed in the uniform flow: (**a**) time history of the fluctuating drag coefficient; (**b**) time history of the lift coefficient; (**c**) the drag coefficient FFT; (**d**) the lift coefficient FFT.

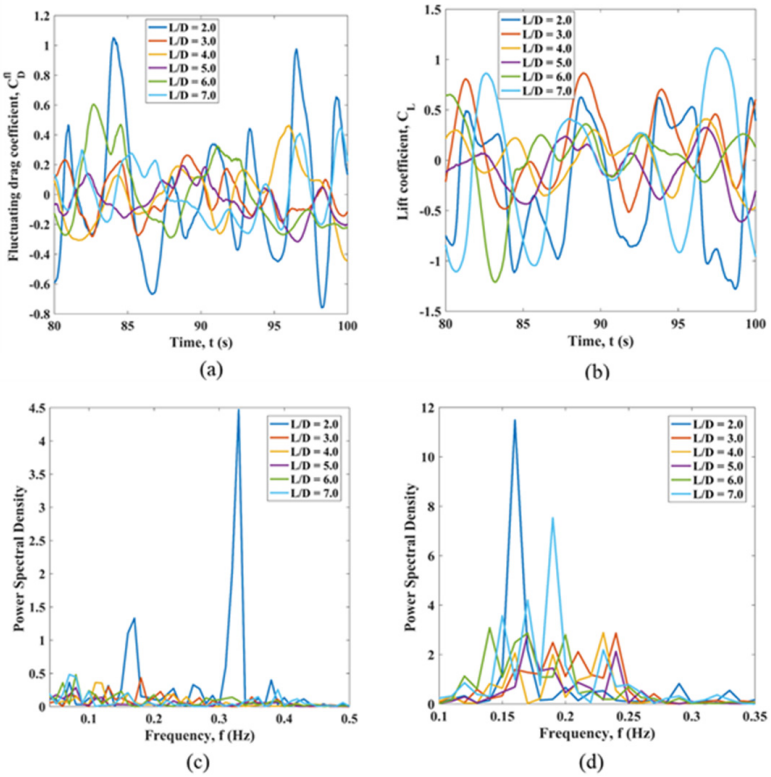

Figure A2. Fluid force coefficients for cylinder 3 immersed in the uniform flow: (**a**) time history of the fluctuating drag coefficient; (**b**) time history of the lift coefficient; (**c**) the drag coefficient FFT; (**d**) the lift coefficient FFT.

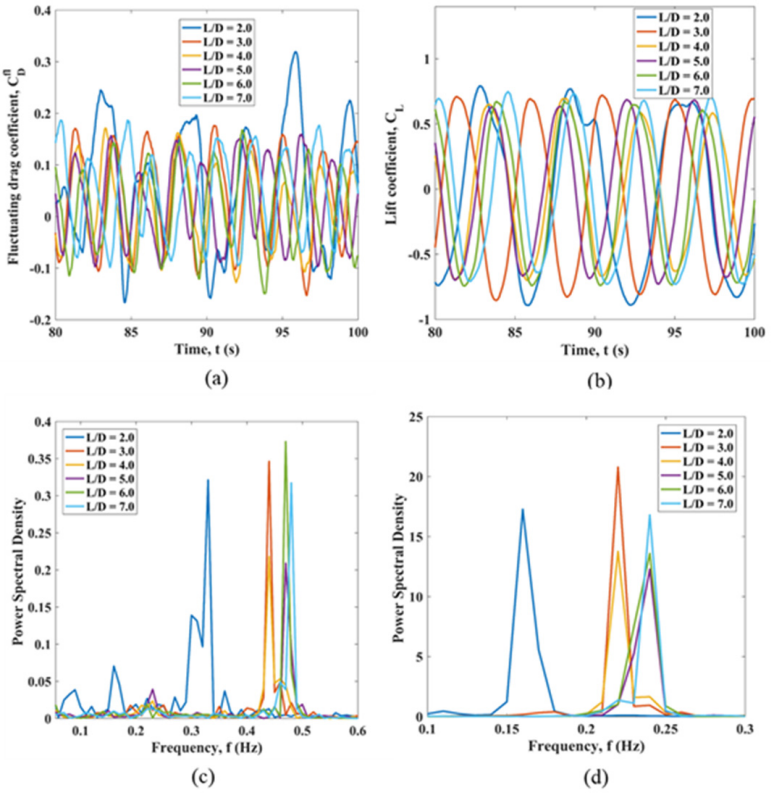

Figure A3. Fluid force coefficients for cylinder 4 immersed in the uniform flow: (**a**) time history of the fluctuating drag coefficient; (**b**) time history of the lift coefficient; (**c**) the drag coefficient FFT; (**d**) the lift coefficient FFT.

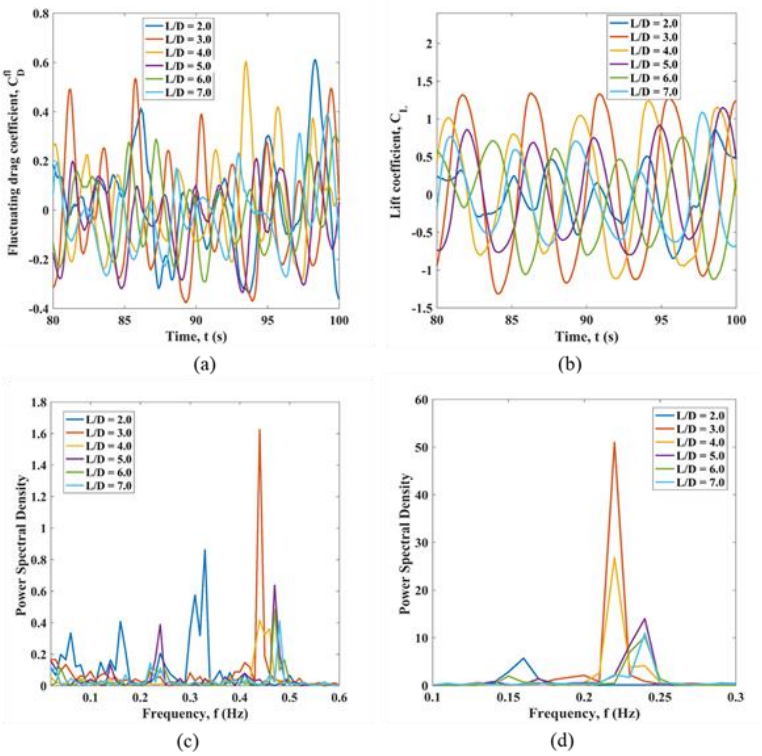

Figure A4. Fluid force coefficients for cylinder 5 immersed in the uniform flow: (**a**) time history of the fluctuating drag coefficient; (**b**) time history of the lift coefficient; (**c**) the drag coefficient FFT; (**d**) the lift coefficient FFT.

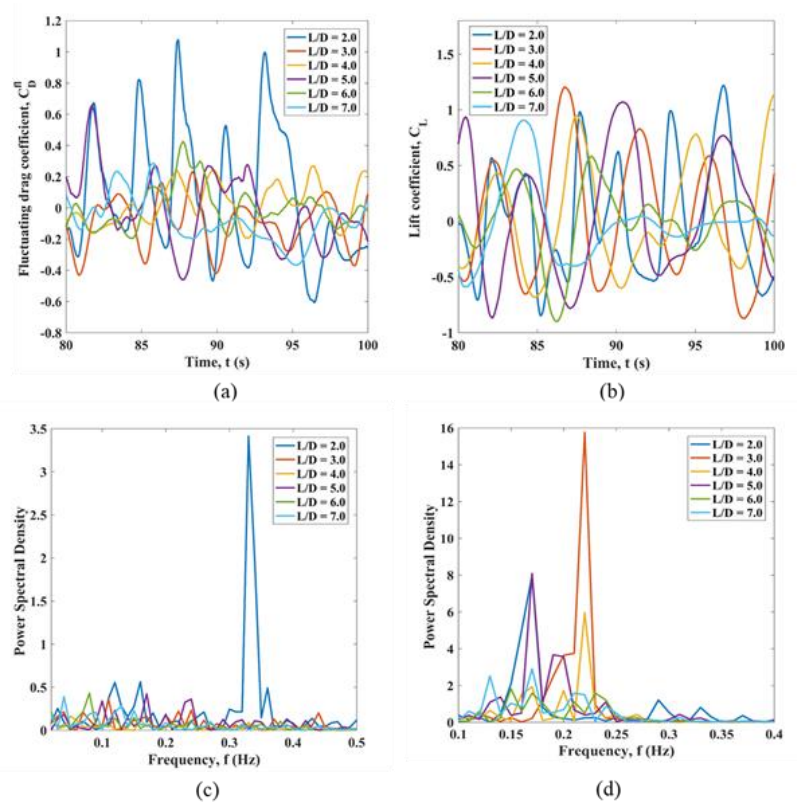

Figure A5. Fluid force coefficients for cylinder 6 immersed in the uniform flow: (**a**) time history of the fluctuating drag coefficient; (**b**) time history of the lift coefficient; (**c**) the drag coefficient FFT; (**d**) the lift coefficient FFT.

Appendix B. Parametric Study for the L/D Variation for Circular Cylinders in Planar Sheared Flow

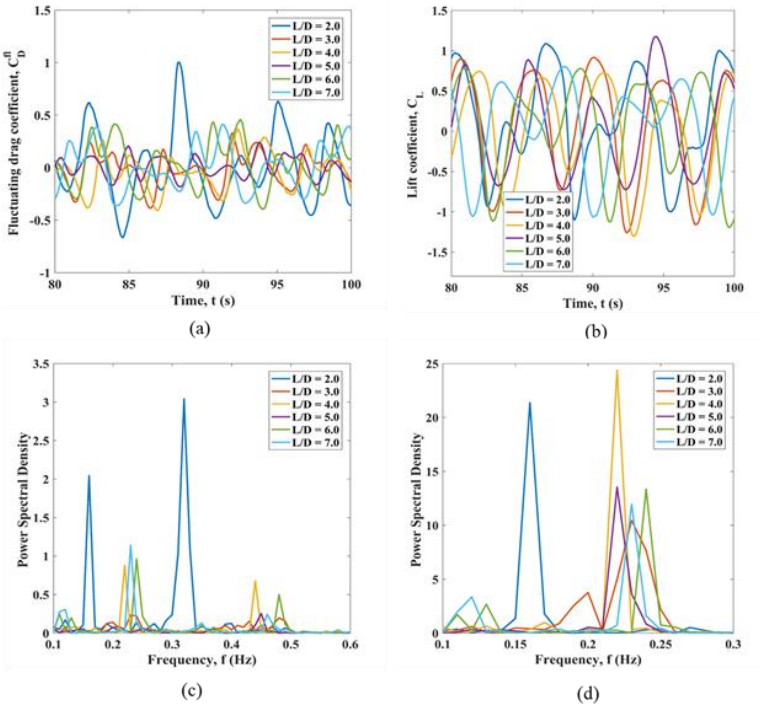

Figure A6. Fluid force coefficients for cylinder 2 immersed in planar sheared flow: (**a**) time history of the fluctuating drag coefficient; (**b**) time history of the lift coefficient; (**c**) the fluctuating drag co–efficient FFT; (**d**) the lift coefficient FFT.

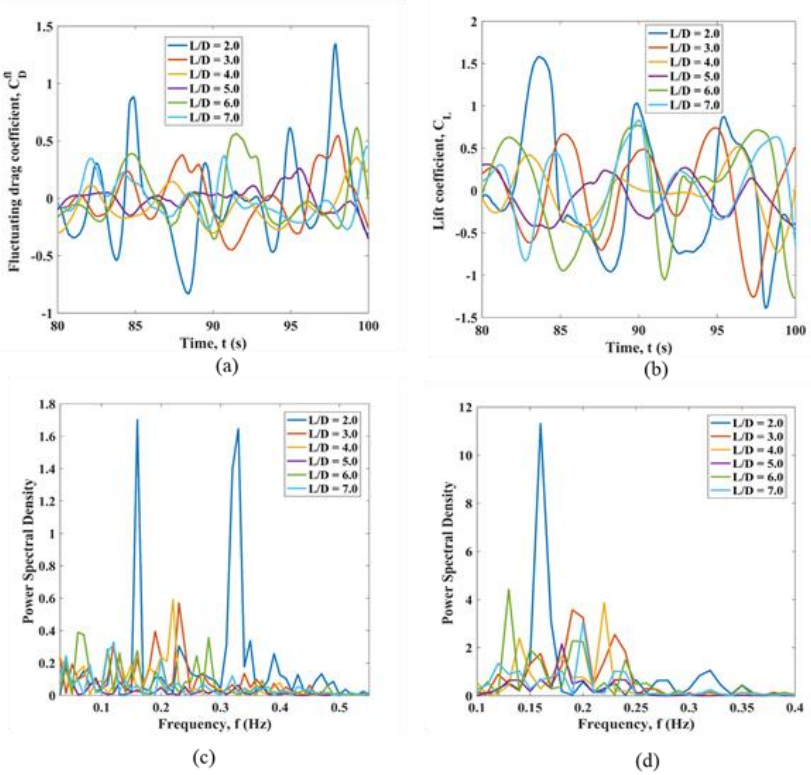

Figure A7. Fluid force coefficients for cylinder 3 immersed in planar sheared flow: (**a**) time history of the fluctuating drag coefficient; (**b**) time history of the lift coefficient; (**c**) the fluctuating drag co–efficient FFT; (**d**) the lift coefficient FFT.

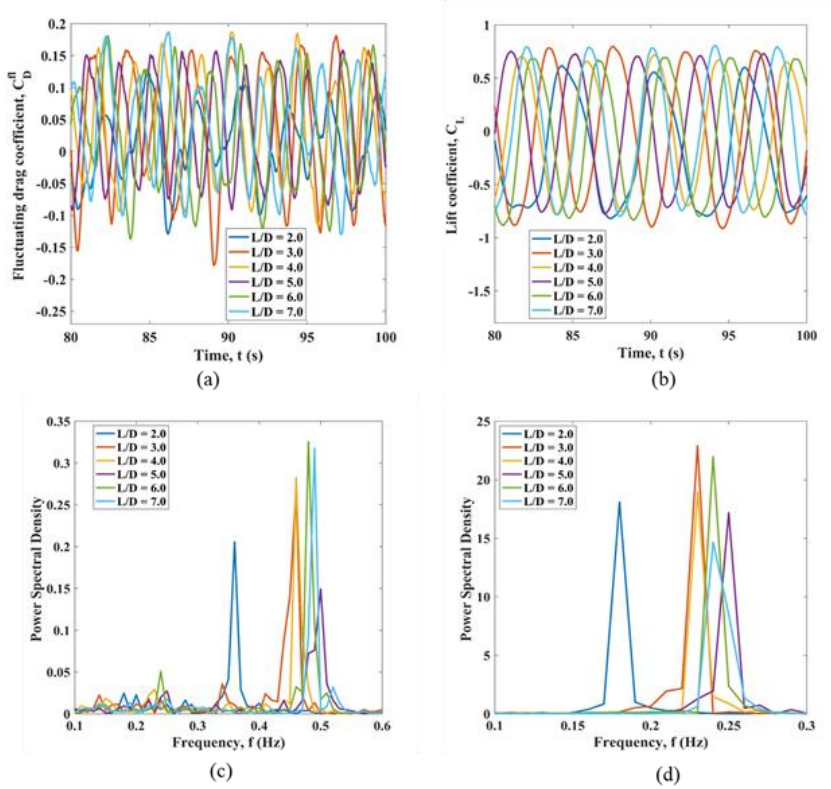

Figure A8. Fluid force coefficients for cylinder 4 immersed in planar sheared flow: (**a**) time history of the fluctuating drag coefficient; (**b**) time history of the lift coefficient; (**c**) the fluctuating drag co–efficient FFT; (**d**) the lift coefficient FFT.

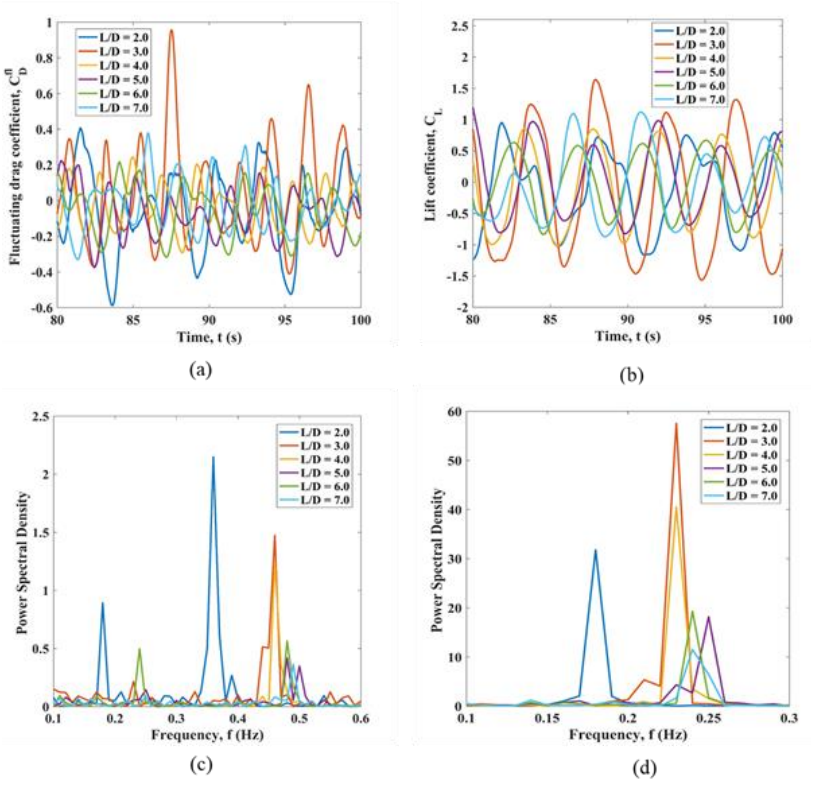

Figure A9. Fluid force coefficients for cylinder 5 immersed in planar sheared flow: (**a**) time history of the fluctuating drag coefficient; (**b**) time history of the lift coefficient; (**c**) the fluctuating drag co–efficient FFT; (**d**) the lift coefficient FFT.

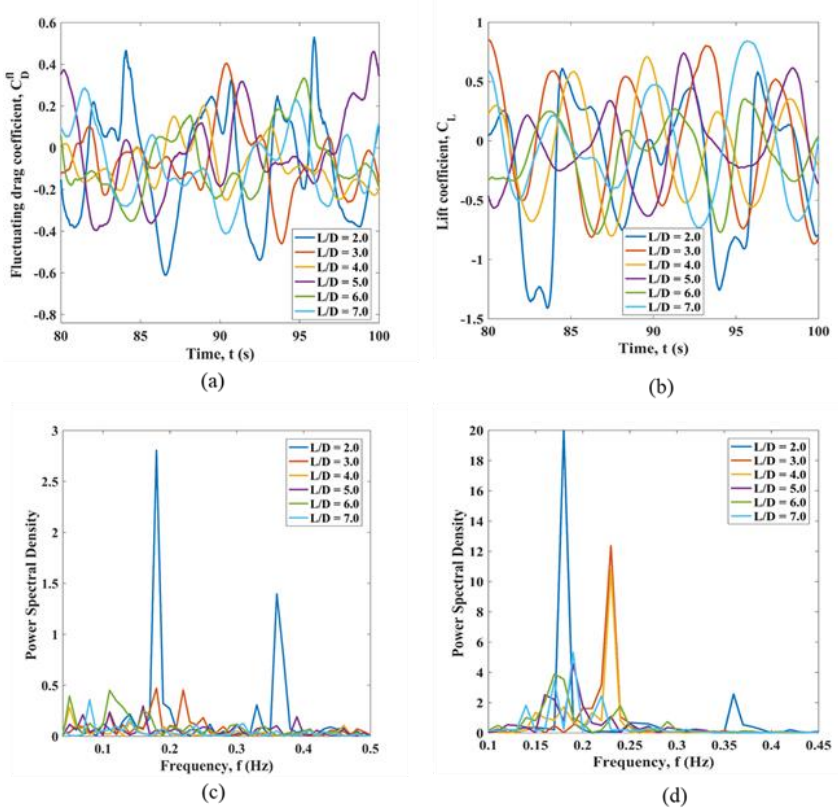

Figure A10. Fluid force coefficients for cylinder 6 immersed in planar sheared flow: (**a**) time history of the fluctuating drag coefficient; (**b**) time history of the lift coefficient; (**c**) the fluctuating drag co–efficient FFT; (**d**) the lift coefficient FFT.

Appendix C. Parametric Study for the Variation of the Cross-Sectional Shape of Cylinders in the Uniform Flow

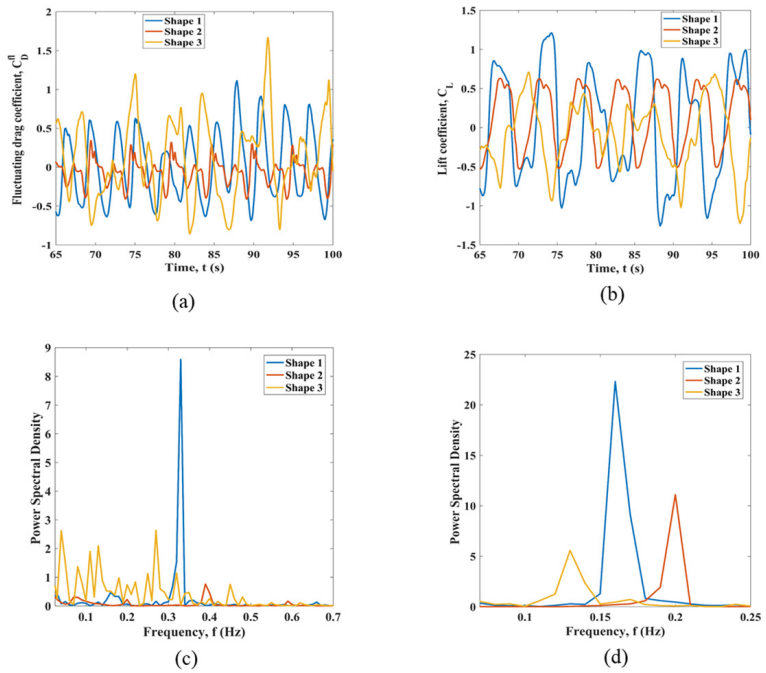

Figure A11. Fluid force coefficients for cylinder 2 immersed in uniform flow: (**a**) time history of the fluctuating drag coefficient; (**b**) time history of the lift coefficient; (**c**) the fluctuating drag coefficient FFT; (**d**) the lift coefficient FFT.

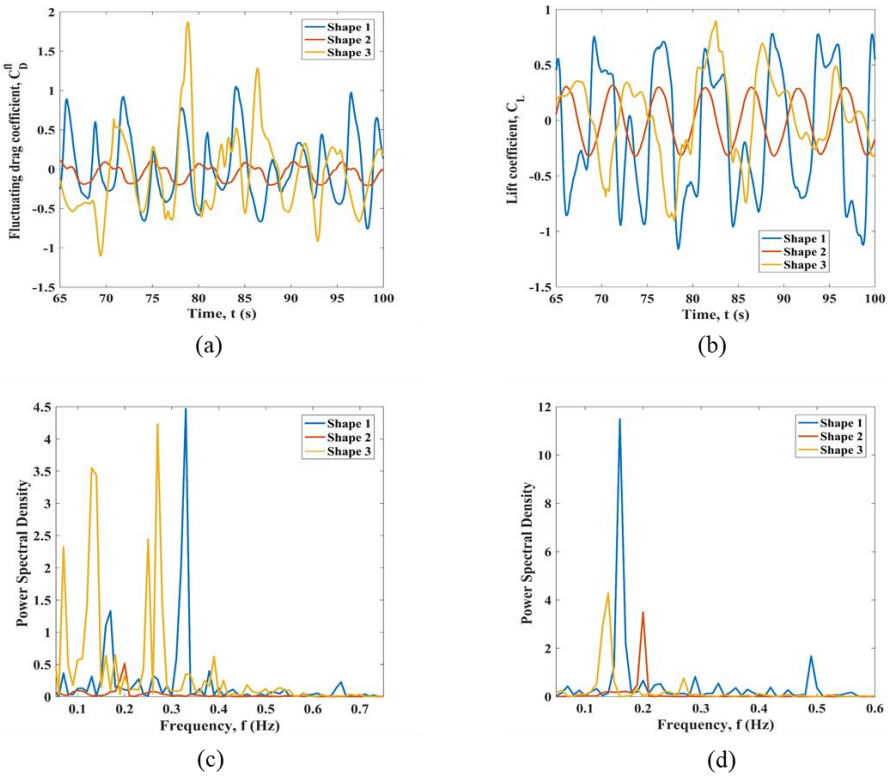

Figure A12. Fluid force coefficients for cylinder 3 immersed in uniform flow: (**a**) time history of the fluctuating drag coefficient; (**b**) time history of the lift coefficient; (**c**) the fluctuating drag coefficient FFT; (**d**) the lift coefficient FFT.

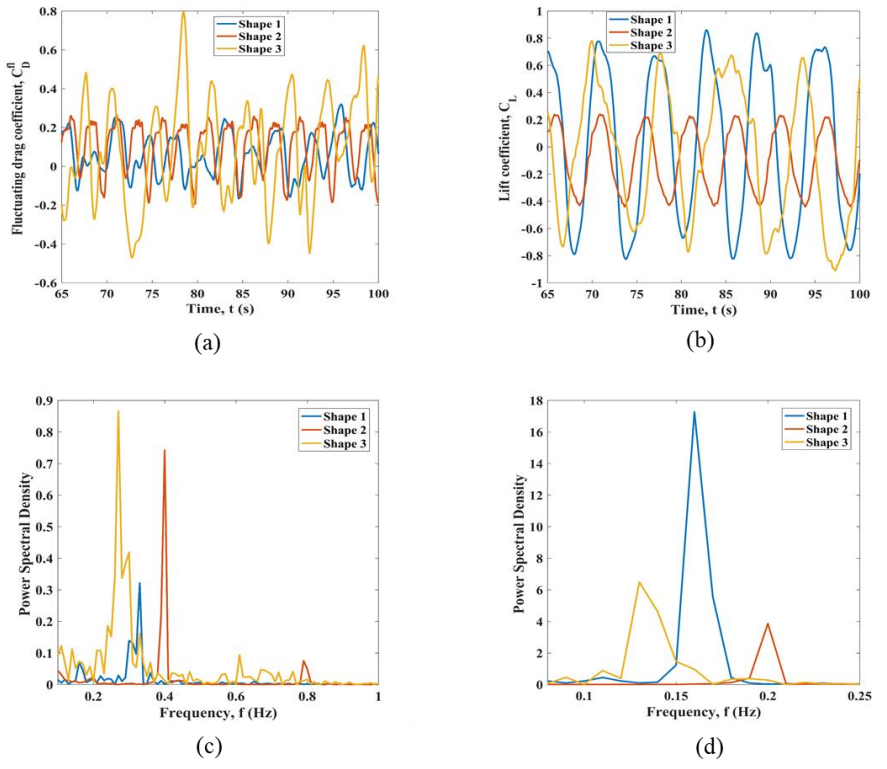

Figure A13. Fluid force coefficients for cylinder 4 immersed in uniform flow: (**a**) time history of the fluctuating drag coefficient; (**b**) time history of the lift coefficient; (**c**) the fluctuating drag coefficient FFT; (**d**) the lift coefficient FFT.

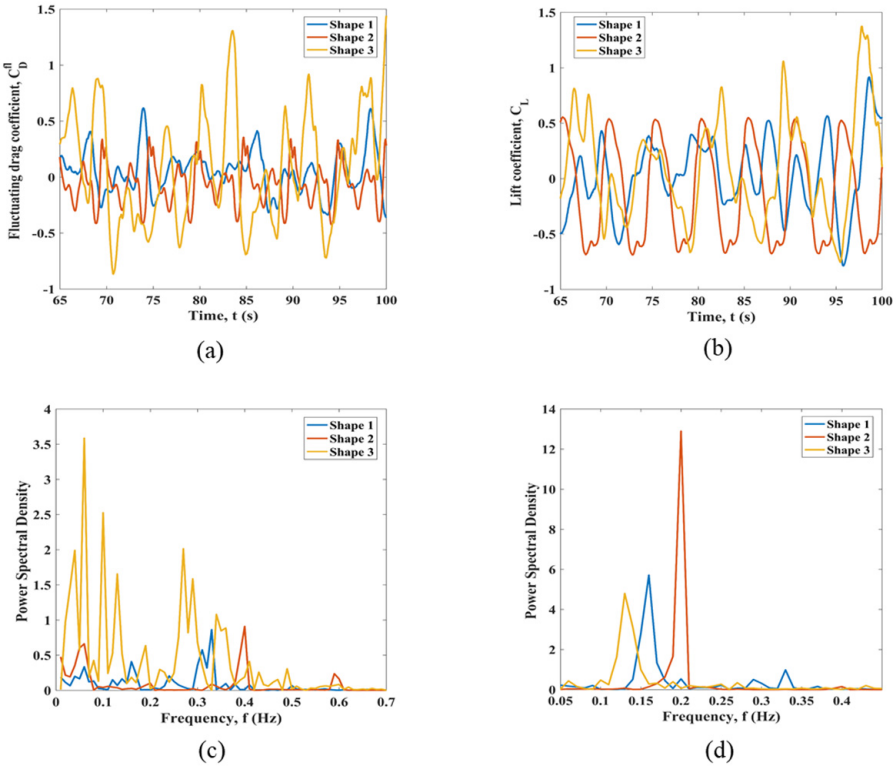

Figure A14. Fluid force coefficients for cylinder 5 immersed in uniform flow: (**a**) time history of the fluctuating drag coefficient; (**b**) time history of the lift coefficient; (**c**) the fluctuating drag coefficient FFT; (**d**) the lift coefficient FFT.

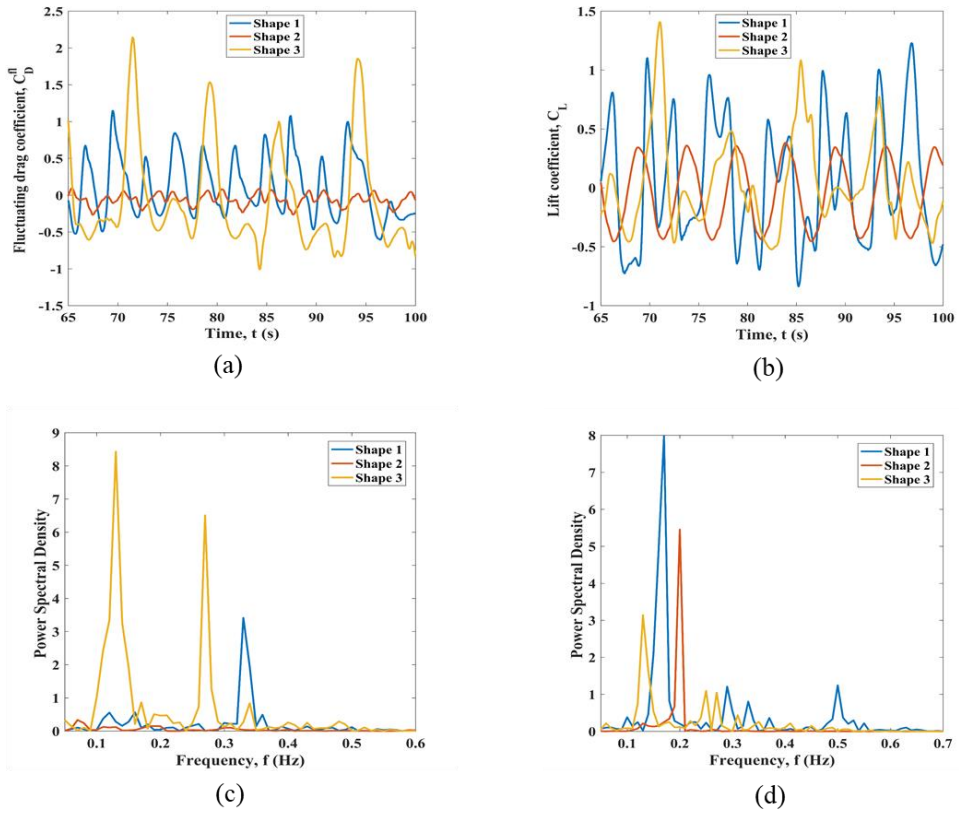

Figure A15. Fluid force coefficients for cylinder 6 immersed in uniform flow: (**a**) time history of the fluctuating drag coefficient; (**b**) time history of the lift coefficient; (**c**) the fluctuating drag coefficient FFT; (**d**) the lift coefficient FFT.

Appendix D. Parametric Study for the Variation of the Cross-Sectional Shape of Cylinders in the Planar Sheared Flow

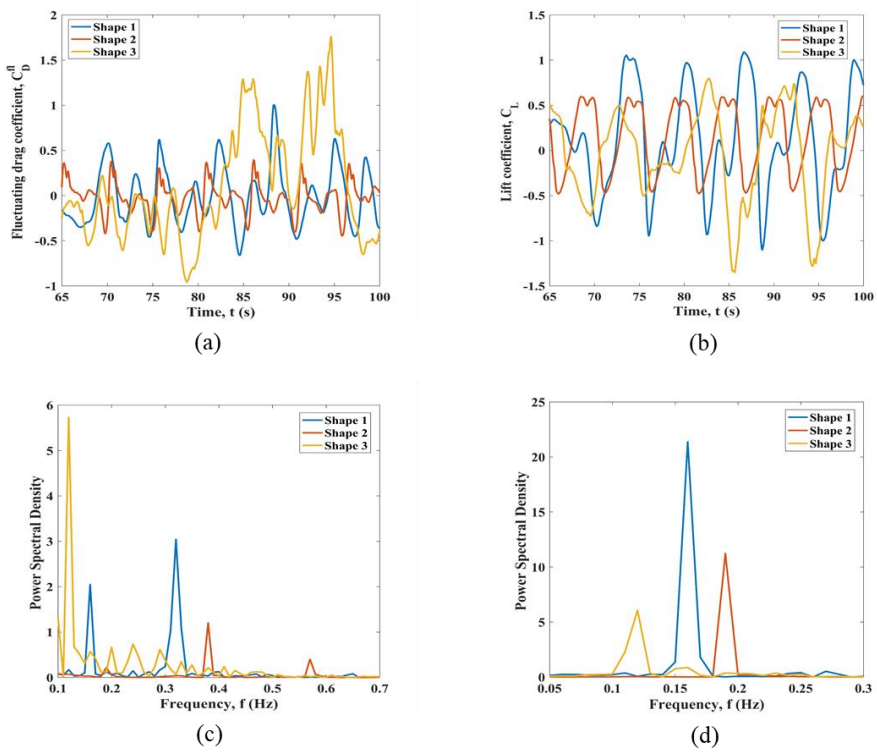

Figure A16. Fluid force coefficients for cylinder 2 immersed in planar sheared flow: (**a**) time history of the fluctuating drag coefficient; (**b**) time history of the lift coefficient; (**c**) the fluctuating drag co–efficient FFT; (**d**) the lift coefficient FFT.

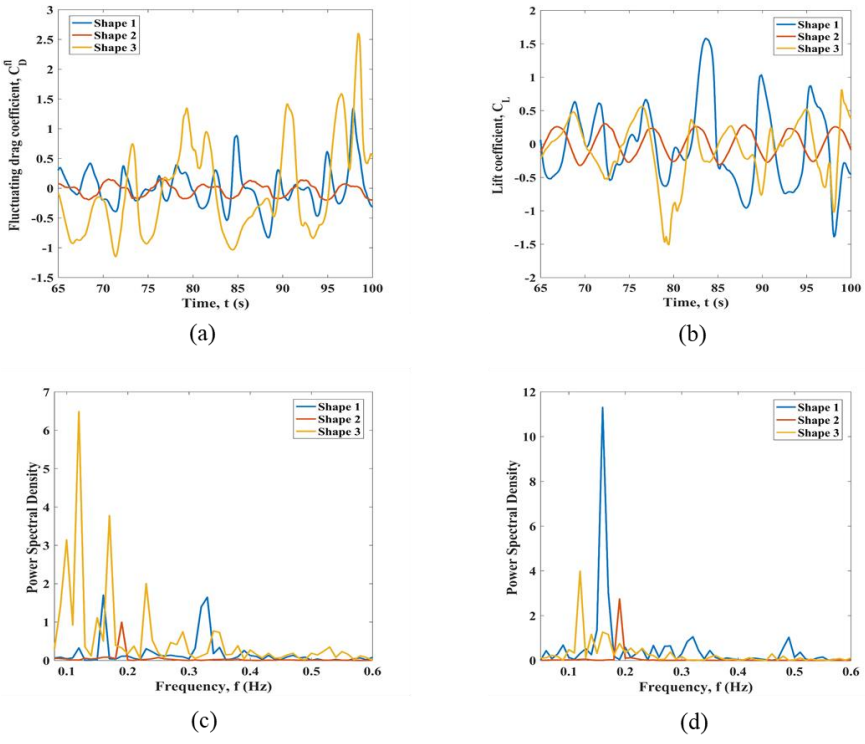

Figure A17. Fluid force coefficients for cylinder 3 immersed in planar sheared flow: (**a**) time history of the fluctuating drag coefficient; (**b**) time history of the lift coefficient; (**c**) the fluctuating drag co–efficient FFT; (**d**) the lift coefficient FFT.

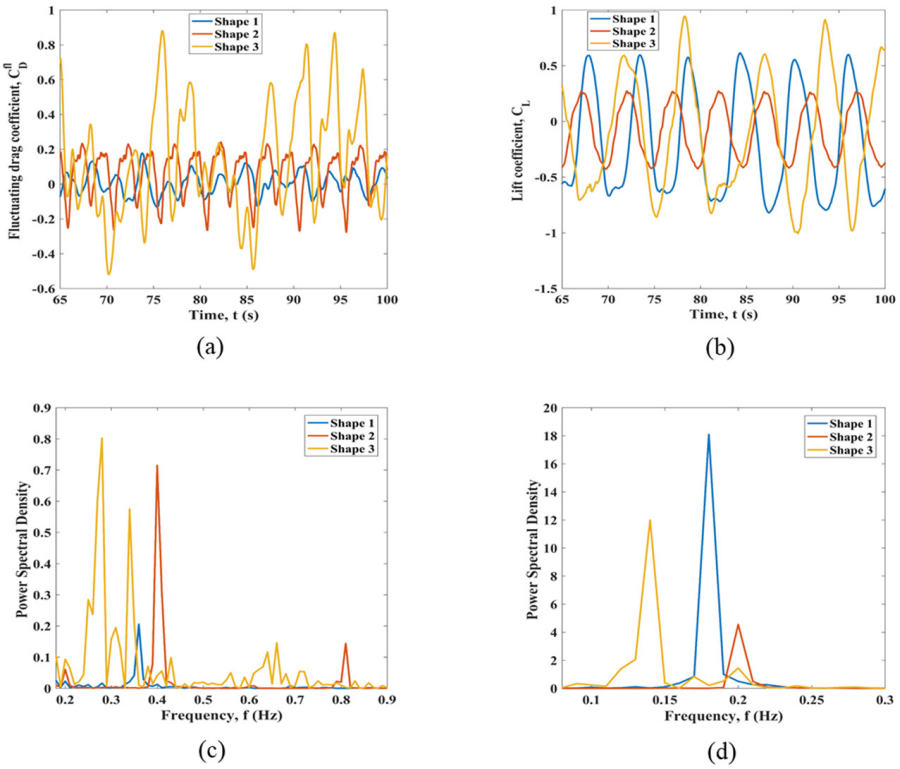

Figure A18. Fluid force coefficients for cylinder 4 immersed in planar sheared flow: (**a**) time history of the fluctuating drag coefficient; (**b**) time history of the lift coefficient; (**c**) the fluctuating drag co–efficient FFT; (**d**) the lift coefficient FFT.

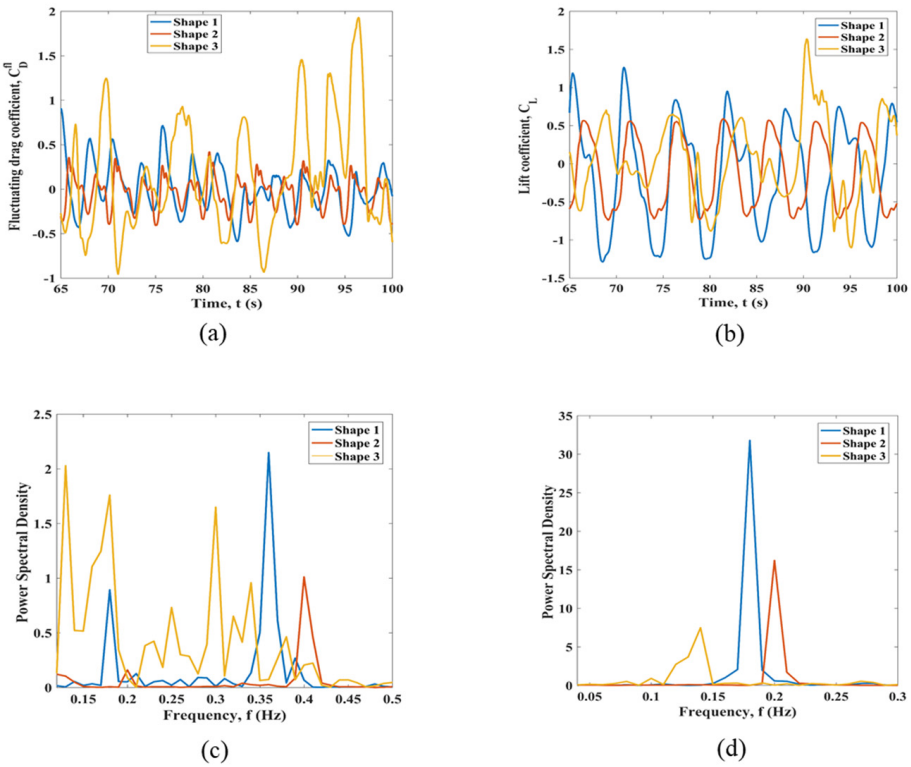

Figure A19. Fluid force coefficients for cylinder 5 immersed in planar sheared flow: (**a**) time history of the fluctuating drag coefficient; (**b**) time history of the lift coefficient; (**c**) the fluctuating drag co–efficient FFT; (**d**) the lift coefficient FFT.

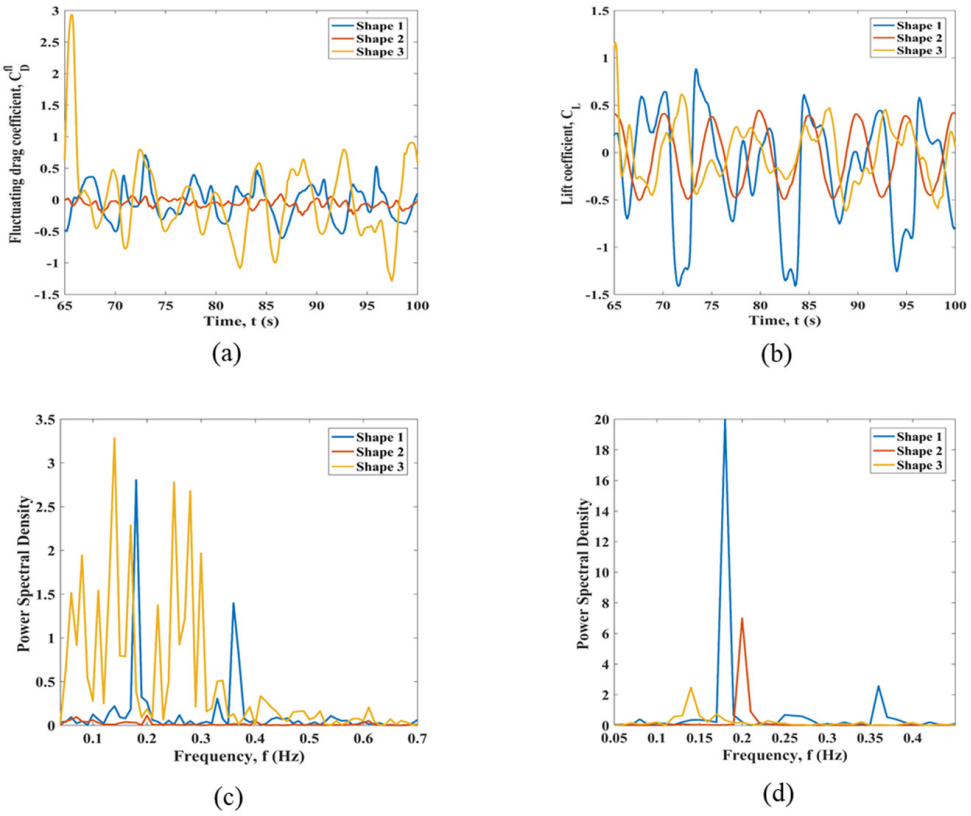

Figure A20. Fluid force coefficients for cylinder 6 immersed in planar sheared flow: (**a**) time history of the fluctuating drag coefficient; (**b**) time history of the lift coefficient; (**c**) the fluctuating drag co–efficient FFT; (**d**) the lift coefficient FFT.

References

1. Zdravkovich, M.M. The effects of interference between circular cylinders in cross flow. *J. Fluids Struct.* **1987**, *1*, 239–261. [CrossRef]
2. Assi, G.R. Mechanisms for Flow-Induced Vibration of Interfering Bluff Bodies. Ph.D. Thesis, Department of Aeronautics, Imperial College London, London, UK, 2009.
3. Assi, G.R.; Bearman, P.W.; Meneghini, J.R. On the wake-induced vibration of tandem circular cylinders: The vortex interaction excitation mechanism. *J. Fluid Mech.* **2010**, *661*, 365–401. [CrossRef]
4. Xu, W.; Haokai, W.; Kun, J.; Enhao, W. Numerical investigation into the effect of spacing on the flow-induced vibrations of two tandem circular cylinders at subcritical Reynolds numbers. *Ocean Eng.* **2021**, *23*, 109521. [CrossRef]
5. Assi, G.D.S.; Bearman, P.W.; Carmo, B.S.; Meneghini, J.R.; Sherwin, S.J.; Willden, R.H.J. The role of wake stiffness on the wake-induced vibration of the downstream cylinder of a tandem pair. *J. Fluid Mech.* **2013**, *718*, 210–245. [CrossRef]
6. Sumner, D.; Richards, M.D.; Akosile, O.O. Two staggered circular cylinders of equal diameter in cross-flow. *J. Fluid. Struct.* **2005**, *20*, 255–276. [CrossRef]
7. Bearman, P.W.; Wadcock, A.J. The interaction between a pair of circular cylinders normal to a stream. *J. Fluid Mech.* **1973**, *61*, 499–511. [CrossRef]
8. Zhang, H.; Melbourne, W.H. Interference between two circular cylinders in tandem in turbulent flow. *J. Wind Eng. Ind. Hydrodyn.* **1992**, *41*, 589–600. [CrossRef]
9. Kitagawa, T.; Ohta, H. Numerical investigation on flow around circular cylinders in tandem arrangement at a subcritical Reynolds number. *J. Fluid. Struct.* **2008**, *24*, 680–699. [CrossRef]
10. Schewe, G.; Jacobs, M. Experiments on the Flow around two tandem circular cylinders from sub-up to trans critical Reynolds numbers. *J. Fluid. Struct.* **2021**, *88*, 148–166. [CrossRef]
11. Annapeh, H.F.; Kurushina, V. Numerical Simulation of Flow-Induced Forces on Subsea Structures in a Group Under Uniform and Sheared Flow. In *International Conference on Wave Mechanics and Vibrations*; Springer Nature: Lisboa, Portugal, 2023; pp. 512–522.
12. Wang, E.; Xu, W.; Yu, Y.; Zhou, L.; Incecik, A. Flow-induced vibrations of three and four long flexible cylinders in tandem arrangement: An experimental study. *Ocean Eng.* **2019**, *178*, 170–184. [CrossRef]
13. Yuhang, Z.; Rui, W.; Yaoran, C.; Yan, B.; Zhaolong, H.; Dai, Z.; Huan, P.; Shixiao, F.; Yongsheng, Z. Three-dimensional wake transition in the flow over four square cylinders at low Reynolds numbers. *AIP Adv.* **2020**, *10*, 015142.

14. Xu, W.; Zhang, S.; Ma, Y.; Liu, B. Fluid forces acting on three and four long side-by-side flexible cylinders undergoing flow-induced vibration (FIV). *Mar. Struct.* **2021**, *75*, 102877. [CrossRef]
15. Gao, Y.; Zhang, Y.; Zhao, M.; Wang, L. Numerical investigation on two degree-of-freedom flow-induced vibration of three tandem cylinders. *Ocean Eng.* **2020**, *201*, 107059. [CrossRef]
16. Zhao, M.; Cheng, L. Numerical simulation of vortex-induced vibration of four circular cylinders in a square configuration. *J. Fluid. Struct.* **2012**, *31*, 125–140. [CrossRef]
17. Han, Z.; Zhou, D.; He, T.; Tu, J.; Li, C.; Kwok, K.C.; Fang, C. Flow-induced vibrations of four circular cylinders with square arrangement at low Reynolds numbers. *Ocean Eng.* **2015**, *96*, 21–33. [CrossRef]
18. Gao, Y.; Yang, K.; Zhang, B.; Cheng, K.; Chen, X. Numerical investigation on vortex-induced vibrations of four circular cylinders in a square configuration. *Ocean Eng.* **2019**, *175*, 223–240. [CrossRef]
19. Gómez, H.A.; Narváez, G.F.; Schettini, E.B. Vortex induced vibration of four cylinders configurations at critical spacing in 0° and 45° flow incidence angle. *Ocean Eng.* **2022**, *252*, 111134. [CrossRef]
20. Ma, Y.; Xu, W.; Liu, B. Dynamic response of three long flexible cylinders subjected to flow-induced vibration (FIV) in an equilateral-triangular configuration. *Ocean Eng.* **2019**, *183*, 187–207. [CrossRef]
21. Liu, Y.; Li, P.; Wang, Y.; Chen, X.; Ren, X.; Lou, M. Dynamic response of five-riser group subjected to vortex-induced vibration in a cylindrical arrangement configuration. *Ocean Eng.* **2022**, *254*, 111271. [CrossRef]
22. Silva-Ortega, M.; Assi, G.R.S. Flow-induced vibration of a circular cylinder surrounded by two, four and eight wake-control cylinders. *Exp. Therm. Fluid Sci.* **2017**, *85*, 354–362. [CrossRef]
23. Assi, G.R.D.S.; Orselli, R.M.; Silva-Ortega, M. Control of vortex shedding from a circular cylinder surrounded by eight rotating wake-control cylinders at Re = 100. *J. Fluid. Struct.* **2019**, *89*, 13–24. [CrossRef]
24. Cicolin, M.M.; Assi, G.R.D.S. Experiments with flexible shrouds to reduce the vortex-induced vibration of a cylinder with low mass and damping. *Appl. Ocean Res.* **2017**, *65*, 290–301. [CrossRef]
25. Assi, G.R.; Crespi, T.; Gharib, M. Novel geometries of serrated helical strakes to suppress vortex-induced vibrations and reduce drag. *Appl. Ocean Res.* **2022**, *120*, 103034. [CrossRef]
26. Gao, Y.; Chen, W.; Wang, B. Numerical simulation of the flow past six-circular cylinders in rectangular configurations. *J. Mar. Sci. Technol.* **2020**, *25*, 718–742. [CrossRef]
27. Arionfard, H.; Mohammadi, S. Numerical Investigation of the Geometrical Effect on Flow-Induced Vibration Performance of Pivoted Bodies. *Energies* **2021**, *14*, 1128. [CrossRef]
28. Wang, Y.-T.; Zhong-min, W.Y.; Hui-min, W. Numerical simulation of low-Reynolds number flows past two tandem cylinders of different diameters. *Water Sci. Eng.* **2013**, *6*, 433–445.
29. Assi, G.R. Wake-induced vibration of tandem cylinders of different diameters. *J. Fluid. Struct.* **2014**, *50*, 329–339. [CrossRef]
30. Zhao, J.; Thompson, M.C.; Hourigan, K. Flow-induced vibration of a D-shape cylinder. In Proceedings of the European Nonlinear Dynamics Conference, Budapest, Hungary, 25–30 June 2017.
31. Assi, G.R.; Bearman, P.W. Vortex-induced vibration of a wavy elliptic cylinder. *J. Fluid. Struct.* **2018**, *80*, 1–21. [CrossRef]
32. Srinil, N. Analysis and prediction of vortex-induced vibrations of variable-tension vertical risers in linearly sheared currents. *Appl. Ocean Res.* **2022**, *33*, 41–53. [CrossRef]
33. Lei, C.; Cheng, L.; Kavanagh, K. A finite difference solution of the shear flow over a circular cylinder. *Ocean Eng.* **2000**, *27*, 271–290. [CrossRef]
34. Wu, T.; Chen, C.-F. Laminar boundary-layer separation over a circular cylinder in uniform shear flow. *Acta Mech.* **2000**, *144*, 71–82. [CrossRef]
35. Sumner, D.; Akosile, O.O. On uniform planar shear flow around a circular cylinder at subcritical Reynolds number. *J Fluid. Struct.* **2003**, *18*, 441–454. [CrossRef]
36. Kang, S. Uniform-shear flow over a circular cylinder at low Reynolds numbers. *J. Fluid. Struct.* **2006**, *22*, 541–555. [CrossRef]
37. Shuyang, C.; Shigehira, O.; Yukio, T.; Yaojun, G.; Hironori, K. Numerical simulation of Reynolds number effects on velocity shear flow around a circular cylinder. *J. Fluid. Struct.* **2010**, *26*, 685–702.
38. Postnikov, A.; Pavlovskaia, E.; Wiercigroch, M. 2DOF CFD calibrated wake oscillator model to investigate vortex-induced vibrations. *Int. J. Mech. Sci.* **2017**, *127*, 176–190. [CrossRef]
39. Nisham, A.; Terziev, M.; Tezdogan, T.; Beard, T.; Incecik, A. Prediction of the aerodynamic behaviour of a full-scale naval ship in head waves using Detached Eddy Simulation. *Ocean Eng.* **2021**, *222*, 108583. [CrossRef]
40. Lehmkuhl, O.; Rodriguez, I.; Borrell, R.; Chiva, J.; Oliva, A. Unsteady forces on a circular cylinder at critical Reynolds number. *Phys. Fluids* **2014**, *12*, 125110. [CrossRef]
41. Achenbach, E.; Heinecke, E. On vortex shedding from smooth and rough cylinders in 33 Forces on a circular cylinder at critical Reynolds. *J. Fluid Mech.* **1981**, *109*, 239–251. [CrossRef]
42. Schewe, G. On the force fluctuations acting on a circular cylinder in cross-flow from subcritical up to transcritical Reynolds numbers. *J. Fluid Mech.* **1983**, *133*, 265–285. [CrossRef]

43. Porteous, A.; Habbit, R.; Colmenares, J.; Poroseva, S.; Murman, S.M. Simulations of incompressible separated turbulent flows around two-dimensional bodies with URANS models in OpenFOAM. In Proceedings of the 22nd AIAA Computational Fluid Dynamics Conference 2015, Dallas, TX, USA, 22–26 June 2015.
44. Nazvanova, A.; Yin, G.; Ong, M.C. Numerical Investigation of Flow around Two Tandem Cylinders in the Upper Transition Reynolds Number Regime Using Modal Analysis. *J. Mar. Sci. Eng.* **2022**, *10*, 1501. [CrossRef]